The Astronomical Journal, 160:267 (21pp), 2020 December https://doi.org/10.3847/1538-3881/abc01b

First Cosmology Results using Supernovae Ia from the Dark Energy Survey: Survey Overview, Performance, and Supernova Spectroscopy

M. Smith[1,2,81], C. B. D'Andrea[3,81], M. Sullivan[1], A. Möller[4], R. C. Nichol[5], R. C. Thomas[6], A. G. Kim[6], M. Sako[3], F. J. Castander[7,8], A. V. Filippenko[9,10], R. J. Foley[11], L. Galbany[12], S. González-Gaitán[13], E. Kasai[14,15], R. P. Kirshner[16,17], C. Lidman[18,19], D. Scolnic[20], D. Brout[3,82], T. M. Davis[21], R. R. Gupta[6], S. R. Hinton[21], R. Kessler[22,23], J. Lasker[22,23], E. Macaulay[5], R. C. Wolf[24], B. Zhang[19], J. Asorey[25], A. Avelino[16], B. A. Bassett[15,26,27], J. Calcino[21], D. Carollo[28], R. Casas[7,8], P. Challis[16], M. Childress[1], A. Clocchiatti[29], S. Crawford[15,30], C. Frohmaier[5], K. Glazebrook[31], D. A. Goldstein[32], M. L. Graham[33], J. K. Hoormann[21], K. Kuehn[34,35], G. F. Lewis[36], K. S. Mandel[37], E. Morganson[38], D. Muthukrishna[19,39], P. Nugent[6], Y.-C. Pan[40], M. Pursiainen[1], R. Sharp[19], N. E. Sommer[19], E. Swann[5], B. P. Thomas[5,41], B. E. Tucker[19], S. A. Uddin[42], P. Wiseman[1], W. Zheng[9], T. M. C. Abbott[43], J. Annis[44], S. Avila[45], K. Bechtol[46], G. M. Bernstein[3], E. Bertin[47,48], D. Brooks[49], D. L. Burke[50,51], A. Carnero Rosell[52,53], M. Carrasco Kind[38,54], J. Carretero[55], C. E. Cunha[50], L. N. da Costa[56,57], C. Davis[50], J. De Vicente[25], H. T. Diehl[44], T. F. Eifler[58,59], J. Estrada[44], J. Frieman[23,44], J. García-Bellido[45], E. Gaztanaga[7,8], D. W. Gerdes[60,61], D. Gruen[50,51,62], R. A. Gruendl[38,54], J. Gschwend[56,57], G. Gutierrez[44], W. G. Hartley[49,63,64], D. L. Hollowood[11], K. Honscheid[65,66], B. Hoyle[67,68,69], D. J. James[70], M. W. G. Johnson[38], M. D. Johnson[38], N. Kuropatkin[44], T. S. Li[71,72], M. Lima[56,73], M. A. G. Maia[56,57], M. March[3], J. L. Marshall[74], P. Martini[65,75,76], F. Menanteau[38,54], C. J. Miller[60,61], R. Miquel[55,77], E. Neilsen[44], R. L. C. Ogando[56,57], A. A. Plazas[71], A. K. Romer[78], E. Sanchez[25], V. Scarpine[44], M. Schubnell[61], S. Serrano[7,8], I. Sevilla-Noarbe[25], M. Soares-Santos[61], F. Sobreira[56,79], E. Suchyta[80], G. Tarle[61], D. L. Tucker[44], and W. Wester[44]

[1] School of Physics and Astronomy, University of Southampton, Southampton, SO17 1BJ, UK; mat.smith@soton.ac.uk
[2] Université de Lyon, F-69622, Lyon, France; Université de Lyon 1, Villeurbanne; CNRS/IN2P3, Institut de Physique des Deux Infinis, Lyon, France
[3] Department of Physics and Astronomy, University of Pennsylvania, Philadelphia, PA 19104, USA
[4] Université Clermont Auvergne, CNRS/IN2P3, LPC, F-63000 Clermont-Ferrand, France
[5] Institute of Cosmology and Gravitation, University of Portsmouth, Portsmouth, PO1 3FX, UK
[6] Lawrence Berkeley National Laboratory, 1 Cyclotron Road, Berkeley, CA 94720, USA
[7] Institut d'Estudis Espacials de Catalunya (IEEC), E-08034 Barcelona, Spain
[8] Institute of Space Sciences (ICE, CSIC), Campus UAB, Carrer de Can Magrans, s/n, 08193 Barcelona, Spain
[9] Department of Astronomy, University of California, Berkeley, CA 94720-3411, USA
[10] Miller Senior Fellow, Miller Institute for Basic Research in Science, University of California, Berkeley, CA 94720, USA
[11] Santa Cruz Institute for Particle Physics, Santa Cruz, CA 95064, USA
[12] Departamento de Física Teórica y del Cosmos, Universidad de Granada, E-18071 Granada, Spain
[13] CENTRA, Instituto Superior Técnico, Universidade de Lisboa, Av. Rovisco Pais 1, 1049-001 Lisboa, Portugal
[14] Department of Physics, University of Namibia, 340 Mandume Ndemufayo Avenue, Pionierspark, Windhoek, Namibia
[15] South African Astronomical Observatory, P.O. Box 9, Observatory 7935, South Africa
[16] Harvard-Smithsonian Center for Astrophysics, 60 Garden Street, Cambridge, MA 02138, USA
[17] Gordon and Betty Moore Foundation, 1661 Page Mill Road, Palo Alto, CA 94304, USA
[18] Centre for Gravitational Astrophysics, College of Science, The Australian National University, ACT 2601, Australia
[19] The Research School of Astronomy and Astrophysics, Australian National University, ACT 2601, Australia
[20] Department of Physics, Duke University Durham, NC 27708, USA
[21] School of Mathematics and Physics, University of Queensland, Brisbane, QLD 4072, Australia
[22] Department of Astronomy and Astrophysics, University of Chicago, Chicago, IL 60637, USA
[23] Kavli Institute for Cosmological Physics, University of Chicago, Chicago, IL 60637, USA
[24] Graduate School of Education, Stanford University, 160, 450 Serra Mall, Stanford, CA 94305, USA
[25] Centro de Investigaciones Energéticas, Medioambientales y Tecnológicas (CIEMAT), Madrid, Spain
[26] African Institute for Mathematical Sciences, 6 Melrose Road, Muizenberg, 7945, South Africa
[27] Department of Maths and Applied Maths, University of Cape Town, Rondebosch, 7700, South Africa
[28] INAF, Astrophysical Observatory of Turin, I-10025 Pino Torinese, Italy
[29] Instituto de Astrofísica, Pontificia Universidad Católica de Chile and ANID—Millennium Science Initiative, Spain
[30] Space Telescope Science Institute, 3700 San Martin Drive, Baltimore, MD 21218, USA
[31] Centre for Astrophysics & Supercomputing, Swinburne University of Technology, Victoria 3122, Australia
[32] California Institute of Technology, 1200 East California Blvd, MC 249-17, Pasadena, CA 91125, USA
[33] Department of Astronomy, University of Washington, Box 351580, U.W., Seattle, WA 98195, USA
[34] Australian Astronomical Optics, Macquarie University, North Ryde, NSW 2113, Australia
[35] Lowell Observatory, 1400 Mars Hill Road, Flagstaff, AZ 86001, USA
[36] Sydney Institute for Astronomy, School of Physics, A28, The University of Sydney, NSW 2006, Australia
[37] Institute of Astronomy and Kavli Institute for Cosmology, Madingley Road, Cambridge, CB3 0HA, UK
[38] National Center for Supercomputing Applications, 1205 West Clark Street, Urbana, IL 61801, USA
[39] Institute of Astronomy, University of Cambridge, Madingley Road, Cambridge CB3 0HA, UK
[40] Graduate Institute of Astronomy, National Central University, 300 Jhongda Road, Zhongli, Taoyuan, 32001, Taiwan
[41] Department of Astronomy, University of Texas at Austin, 2515 Speedway, Stop C1400 Austin, TX, USA
[42] McDonald Observatory, The University of Texas at Austin, Fort Davis, TX 79734, USA
[43] Cerro Tololo Inter-American Observatory, NSF's National Optical-Infrared Astronomy Research Laboratory, Casilla 603, La Serena, Chile
[44] Fermi National Accelerator Laboratory, P.O. Box 500, Batavia, IL 60510, USA
[45] Instituto de Fisica Teorica UAM/CSIC, Universidad Autonoma de Madrid, 28049 Madrid, Spain
[46] Physics Department, 2320 Chamberlin Hall, University of Wisconsin-Madison, 1150 University Avenue, Madison, WI 53706-1390
[47] CNRS, UMR 7095, Institut d'Astrophysique de Paris, F-75014, Paris, France
[48] Sorbonne Universités, UPMC Univ Paris 06, UMR 7095, Institut d'Astrophysique de Paris, F-75014, Paris, France
[49] Department of Physics & Astronomy, University College London, Gower Street, London, WC1E 6BT, UK

[50] Kavli Institute for Particle Astrophysics & Cosmology, P.O. Box 2450, Stanford University, Stanford, CA 94305, USA
[51] SLAC National Accelerator Laboratory, Menlo Park, CA 94025, USA
[52] Instituto de Astrofisica de Canarias, E-38205 La Laguna, Tenerife, Spain
[53] Universidad de La Laguna, Dpto. Astrofísica, E-38206 La Laguna, Tenerife, Spain
[54] Department of Astronomy, University of Illinois at Urbana-Champaign, 1002 W. Green Street, Urbana, IL 61801, USA
[55] Institut de Física d'Altes Energies (IFAE), The Barcelona Institute of Science and Technology, Campus UAB, E-08193 Bellaterra (Barcelona) Spain
[56] Laboratório Interinstitucional de e-Astronomia—LIneA, Rua Gal. José Cristino 77, Rio de Janeiro, RJ—20921-400, Brazil
[57] Observatório Nacional, Rua Gal. José Cristino 77, Rio de Janeiro, RJ—20921-400, Brazil
[58] Department of Astronomy/Steward Observatory, University of Arizona, 933 North Cherry Avenue, Tucson, AZ 85721-0065, USA
[59] Jet Propulsion Laboratory, California Institute of Technology, 4800 Oak Grove Drive, Pasadena, CA 91109, USA
[60] Department of Astronomy, University of Michigan, Ann Arbor, MI 48109, USA
[61] Department of Physics, University of Michigan, Ann Arbor, MI 48109, USA
[62] Department of Physics, Stanford University, 382 Via Pueblo Mall, Stanford, CA 94305, USA
[63] Département de Physique Théorique and Center for Astroparticle Physics, Université de Genève, 24 quai Ernest Ansermet, CH-1211 Geneva, Switzerland
[64] Department of Physics, ETH Zurich, Wolfgang-Pauli-Strasse 16, CH-8093 Zurich, Switzerland
[65] Center for Cosmology and Astro-Particle Physics, The Ohio State University, Columbus, OH 43210, USA
[66] Department of Physics, The Ohio State University, Columbus, OH 43210, USA
[67] Faculty of Physics, Ludwig-Maximilians-Universität, Scheinerstr. 1, D-81679 Munich, Germany
[68] Max Planck Institute for Extraterrestrial Physics, Giessenbachstrasse, D-85748 Garching, Germany
[69] Universitäts-Sternwarte, Fakultät für Physik, Ludwig-Maximilians Universität München, Scheinerstr. 1, 81679 München, Germany
[70] Center for Astrophysics | Harvard & Smithsonian, 60 Garden Street, Cambridge, MA 02138, USA
[71] Department of Astrophysical Sciences, Princeton University, Peyton Hall, Princeton, NJ 08544, USA
[72] Observatories of the Carnegie Institution for Science, 813 Santa Barbara Street, Pasadena, CA 91101, USA
[73] Departamento de Física Matemática, Instituto de Física, Universidade de São Paulo, CP 66318, São Paulo, SP, 05314-970, Brazil
[74] George P. and Cynthia Woods Mitchell Institute for Fundamental Physics and Astronomy, and Department of Physics and Astronomy, Texas A&M University, College Station, TX 77843, USA
[75] Department of Astronomy, The Ohio State University, Columbus, OH 43210, USA
[76] Radcliffe Institute for Advanced Study, Harvard University, Cambridge, MA 02138, USA
[77] Institució Catalana de Recerca i Estudis Avançats, E-08010 Barcelona, Spain
[78] Department of Physics and Astronomy, Pevensey Building, University of Sussex, Brighton, BN1 9QH, UK
[79] Instituto de Física Gleb Wataghin, Universidade Estadual de Campinas, 13083-859, Campinas, SP, Brazil
[80] Computer Science and Mathematics Division, Oak Ridge National Laboratory, Oak Ridge, TN 37831, USA
Received 2020 July 28; revised 2020 October 7; accepted 2020 October 10; published 2020 November 18

Abstract

We present details on the observing strategy, data-processing techniques, and spectroscopic targeting algorithms for the first three years of operation for the Dark Energy Survey Supernova Program (DES-SN). This five-year program using the Dark Energy Camera mounted on the 4 m Blanco telescope in Chile was designed to discover and follow supernovae (SNe) Ia over a wide redshift range ($0.05 < z < 1.2$) to measure the equation-of-state parameter of dark energy. We describe the SN program in full: strategy, observations, data reduction, spectroscopic follow-up observations, and classification. From three seasons of data, we have discovered 12,015 likely SNe, 308 of which have been spectroscopically confirmed, including 251 SNe Ia over a redshift range of $0.017 < z < 0.85$. We determine the effective spectroscopic selection function for our sample and use it to investigate the redshift-dependent bias on the distance moduli of SNe Ia we have classified. The data presented here are used for the first cosmology analysis by DES-SN ("DES-SN3YR"), the results of which are given in Dark Energy Survey Collaboration et al. The 489 spectra that are used to define the DES-SN3YR sample are publicly available at https://des.ncsa.illinois.edu/releases/sn.

Unified Astronomy Thesaurus concepts: Type Ia supernovae (1728); Supernovae (1668); Cosmology (343); Cosmological parameters (339); Observational cosmology (1146); Sky surveys (1464)

1. Introduction

Supernovae (SNe) Ia have fundamentally changed our understanding of the universe. It is through their utility as accurate distance indicators that the High-Z Supernova Search Team (Riess et al. 1998) and the Supernova Cosmology Project (Perlmutter et al. 1999) were able to make the groundbreaking discovery that the expansion of the universe is accelerating. To date, the cause of this phenomenon, commonly referred to as "dark energy," remains unknown.

The quest for understanding the cause of the acceleration and constraining the models that describe it have motivated ever-improving SN searches over the past two decades. At redshift $z \leqslant 1$ these cosmology-oriented programs include the Supernova Legacy Survey (SNLS; Conley et al. 2011), the Sloan Digital Sky Survey-II Supernova Program (SDSS-II; Frieman et al. 2008), and more recently, Pan-STARRS (Tonry et al. 2012; Rest et al. 2014). The low-redshift sample necessary for anchoring the Hubble diagram includes SNe Ia heterogeneously collated from the Calán/Tololo survey (Hamuy et al. 1996), several Harvard-Smithsonian Center for Astrophysics (CfA) surveys (Riess et al. 1999; Jha et al. 2006; Hicken et al. 2009, 2012), the Carnegie Supernova Project (CSP; Contreras et al. 2010; Stritzinger et al. 2011; Krisciunas et al. 2017), the Lick Observatory Supernova Search (Ganeshalingam et al. 2010; Stahl et al. 2019), and (more recently) the homogeneous Foundation Survey (Foley et al. 2018). Nearly all observations of SNe Ia at $z > 1.1$ are obtained from space with a few dozen well-observed objects to date (Suzuki et al. 2012; Riess et al. 2018; Williams et al. 2020).

The surveys described above all obtain distance measurements from light-curve fits to cadenced multicolor photometry

[81] The authors contributed equally to this work.
[82] NASA Einstein Fellow.

(Riess et al. 1996; Guy et al. 2010). But to define the sample of SNe Ia used in a cosmological analysis requires a parallel spectroscopic follow-up program. Real-time spectroscopy allows the survey to robustly differentiate observed transients between SNe Ia and other classes of SNe, while also obtaining precise redshifts for the objects. Thus, the spectroscopic program determines what data are included in a Hubble diagram as well as the position of these data along the redshift axis. For high-redshift ($z > 0.2$) SN surveys, the spectroscopic program traditionally requires more observing time on larger facilities than the entire photometric observing program.

In this paper we give an overview of the Dark Energy Survey —Supernova Program (DES-SN), and describe the SN spectroscopy program used in the first three seasons of the survey. These observations define the base sample used in the first cosmological analysis of spectroscopically classified SNe Ia from DES-SN ("DES-SN3YR"). This paper is one in a series (Kessler et al. 2015; Gupta et al. 2016; Kessler & Scolnic 2017; Brout et al. 2019a; Lasker et al. 2019; Kessler et al. 2019; Smith et al. 2020) that combine to produce cosmological constraints from DES-SN alone (Dark Energy Survey Collaboration et al. 2019b; Brout et al. 2019b; Hinton et al. 2019; Macaulay et al. 2019) and in combination with other DES probes (Dark Energy Survey Collaboration et al. 2019a).

The format of the paper is as follows. In Section 2 we describe the strategy and status of the overall DES-SN observing program. Section 3 explains how SN candidates are defined and extracted from the data, while Section 4 details the spectroscopic follow-up campaign for each observatory used in our program. In Section 5 we derive the effective spectroscopic selection function from the classifications obtained by our program, essential for understanding the biases in a spectroscopically derived SN Hubble diagram from DES. We conclude in Section 6 by looking toward future releases and analyses of DES data.

2. The DES Supernova Program

2.1. Dark Energy Survey

The Dark Energy Survey (Dark Energy Survey Collaboration et al. 2016) was a 6 yr, ~570 night survey using the 4 m Blanco telescope at Cerro Tololo Inter-American Observatory (CTIO) in Chile. It used the Dark Energy Camera (DECam; Flaugher et al. 2015), a 520 megapixel wide-field imager with a 2.2° field of view and deep-depleted CCDs, giving it excellent quantum efficiency out to 1 μm. Commissioning of the camera began in 2012 September and a period of data-taking by DES called Science Verification ("SV") was carried out from 2012 November through 2013 February. The first season of the survey ("Y1") began on 2013 August 31 and the third season ("Y3") ended on 2016 February 12.

DES is split into two distinct observing modes: the wide-area survey (DES-wide), observing 5000 square degrees in *grizY* to a 5σ depth of $i \approx 23.5$ mag, and DES-SN. The observing strategy for DES-SN is optimized for the purposes of SN Ia cosmology. DES-SN is a 10-field hybrid-depth survey, designed to obtain a few thousand well-observed light curves of SNe Ia over a redshift range $0.2 < z < 1.2$.

There are three defining aspects of DES-SN. The first is the excellent *z*-band response of DECam owing to the deep-depleted CCDs (Diehl et al. 2014). This allows for rest-frame optical light curves of $z \approx 1$ SNe Ia to be well measured. The second is excellent calibration, as this has been the largest systematic uncertainty in SN Ia cosmology (Scolnic et al. 2018). The DES Science Requirements state that the survey must be calibrated to 0.5% in its absolute calibrations and colors.

The third defining aspect is photometric classification of SNe Ia. The field of view of DECam is much larger than that of any previous camera on a similarly sized telescope, allowing DES-SN to observe an unprecedented area for its depth. Thus, given the quantity of faint SNe that DES-SN discovers, any realistic spectroscopic resource allocation will only permit spectroscopic classification for a small fraction of these SNe. To make optimal use of the DES-SN data, the final analysis of this data set will rely on photometric classification for our primary cosmology analysis. This does not remove the need for spectroscopic follow-up observations of live SNe, but rather places different priorities on the follow-up program, as explained in Section 4.

In the remainder of this section we first describe in detail the first three seasons of the DES-SN observing program.

Table 1
Exposure Times

Filter	Shallow Field			Deep Field		
	t_{exp}[a]	N_{exp}[b]	Depth[c]	t_{exp}[a]	N_{exp}[b]	Depth[c]
g	175	1	23.7	600	3	24.6
r	150	1	23.6	1200	3	24.8
i	200	1	23.5	1800	5	24.7
z	400	2	23.3	3630	11	24.4

Notes.
[a] Total exposure time per filter epoch (in seconds).
[b] Number of exposures per filter epoch.
[c] Median limiting magnitude per pointing over the first three seasons of DES-SN, defined as the magnitude at which 50% of fake SNe inserted into the pipeline are recovered by difference imaging (Kessler et al. 2015).

2.2. Exposure Time and Depth

DES-SN has fields of two different depths: eight "shallow" and two "deep" fields, with limiting AB magnitudes of ~23.5 and ~24.5, respectively, where each field is a single pointing of DECam. The deep fields serve to extend the redshift range of cosmologically useful SNe Ia out to $z \approx 1.2$, while the more numerous shallow fields add volume and numbers at intermediate redshifts. The total exposure time for each filter and the median limiting magnitude for both the deep and shallow fields are given in Table 1. Longer observations are split into a number of shorter exposures and coadded (e.g., 11 exposures for the 1 hr per epoch *z*-band deep fields). Limiting magnitudes for each observation are derived from artificially inserting SNe into our processing pipeline and determining the magnitude at which 50% of all such objects are recovered (Kessler et al. 2015). Derived directly from the data, these limits take into account real observing conditions. Throughout the text, we refer to an observation of one field, in one filter, on one night, as a "filter epoch."

DECam has a 2°.2 diameter field of view and an observable area (excluding chip gaps) of 2.7 deg^2. Considering masked pixels, dead CCDs, and field overlaps, the DES-SN program covered a total effective observing area of 23 deg^2, nearly six

Table 2
Field Locations

Legacy Field	DES ID	R.A. [time]	Decl. [deg]	R.A. [deg]	Decl. [deg]
CDFS	C1	$03^h\ 37^m\ 05\overset{s}{.}83$	−27:06:41.8	54.2743	−27.1116
	C2	$03^h\ 37^m\ 05\overset{s}{.}83$	−29:05:18.2	54.2743	−29.0884
	C3	$03^h\ 30^m\ 35\overset{s}{.}62$	−28:06:00.0	52.6484	−28.1000
Elais-S1	E1	$00^h\ 31^m\ 29\overset{s}{.}86$	−43:00:34.6	7.8744	−43.0096
	E2	$00^h\ 38^m\ 00\overset{s}{.}00$	−43:59:52.8	9.5000	−43.9980
SDSS Stripe 82	S1	$02^h\ 51^m\ 16\overset{s}{.}80$	00:00:00.0	42.8200	0.0000
	S2	$02^h\ 44^m\ 46\overset{s}{.}66$	−00:59:18.2	41.1944	−0.9884
XMM-LSS	X1	$02^h\ 17^m\ 54\overset{s}{.}17$	−04:55:46.2	34.4757	−4.9295
	X2	$02^h\ 22^m\ 39\overset{s}{.}48$	−06:24:43.6	35.6645	−6.4121
	X3	$02^h\ 25^m\ 48\overset{s}{.}00$	−04:36:00.0	36.4500	−4.6000

Note. RA and DEC given in J2000 coordinates.

times the area of SNLS. DES-SN does not dither over the gaps, since filling these in decreases the area repeatedly observed on the subsequent epoch. Dithers on the order of a few arcseconds are carried out, allowing instrumental artifacts to be corrected in processing. Since dithers do not cross the chip gap, any object in a field appears on only one chip for all DES-SN exposures; therefore, our processing pipeline treats each chip independently.

2.3. Field Locations

The 10 DES-SN fields are grouped in 4 distinct regions of the sky, coinciding with well-observed legacy fields. Each region contains two adjacent shallow fields and in two of the four regions there is also an adjacent deep field.

The prefix for each DES field name is derived from the name of the legacy field in which it is located: "X" for the fields lying in the XMM-LSS (Pierre et al. 2004) footprint, "C" for the fields clustered around the Chandra Deep Field—South (CDFS; Giacconi et al. 2001), "E" for the fields in and around Elais-S1 (Rowan-Robinson et al. 2004), and "S" for fields located in SDSS—Stripe 82 (Adelman-McCarthy et al. 2007). The centroids of each field are given in Table 2. Shallow fields have a suffix of 1 or 2, with the more northerly field given the designation 1. Deep fields have a suffix of 3. All fields in the same region contain a small (∼1%) amount of overlap with one another.

The DES-SN fields lie within the DES-wide footprint to benefit from a consistent photometric calibration (Figure 1). This constraint forces all fields to be relatively close in R.A. (RA), spanning only three hours. The fields are broadly distributed in decl. in order to allow for spectroscopic follow-up observations at low airmass from northern observatories for half of the fields (X and S), while the C and E fields are more southerly to allow for longer windows at low airmass and better avoidance of the Moon.

In addition to considerations of calibration and spectroscopic follow-up observations, the DES-SN fields were selected with Milky Way extinction and ancillary data in mind. Eight of 10 fields are located in low-extinction regions where ($E(B-V) < 0.02$ mag). The DES-SN fields overlap with deep near-infrared (VIDEO; Jarvis et al. 2013) and mid-infrared (SWIRE; Lonsdale et al. 2003) survey regions, with field centroids optimized to minimize the area lost from masking of bright stars and their bleed trails.

2.4. Observing Strategy

DES observed in seasons, ∼5.5 months long, starting in mid- to late August and ending in early to mid-February. The season is constrained from being extended by the requirement of low-airmass observations in the compact DES-wide footprint. The length of the continuous observing season helps to reduce the fraction of truncated DES-SN light curves, particularly for highly time-dilated SNe at $z \geqslant 1$. Most DES nights are dark, but CTIO scheduled gray and bright time for DES as well to provide the wider community with access to DECam during dark time throughout the year. As such, the structure of DES-SN observations—survey duration, cadence, sky brightness—are the result of these competing interests.

DES uses an algorithmic scheduler (`ObsTac`; Neilsen & Annis 2014) to determine the survey program (DES-SN or DES-wide), field, and filter to observe given the apparent observing conditions, the completeness of the DES-wide footprint, and the length of time $\Delta t_{\rm seq}$ since the last accepted observation of each DES-SN sequence. A "sequence" is defined as a series of exposures that are not interrupted once they begin, regardless of changing conditions. The number of exposures per filter, per field is listed in Table 1. For each of the DES-SN shallow fields a sequence is all of the exposures in all of the filters (*grizz*) with a total exposure time of 15 min. For the DES-SN deep fields, each filter epoch is treated as a distinct sequence in each filter (i.e., *ggg*, *rrr*, *iiiii* or *zzzzzzzzzz*), with exposure times of 10, 20, 30, and 60 min, respectively. This uncoupling of the long deep field filter epochs introduces scheduling flexibility for `ObsTac` to better optimize observations.

A DES-SN sequence is triggered if $\Delta t_{\rm seq} \geqslant 4$d and the seeing (measured at zenith in the i band) is $\geqslant 1\farcs1$ or with no lower limit on the seeing if $\Delta t_{\rm seq} \geqslant 7$ days. Priority is always given to the sequence with the largest $\Delta t_{\rm seq}$. There are upper limits on the projected seeing for the deep ($1\farcs3$) and shallow ($1\farcs8$) fields to minimize poor-quality data. DES-SN observations require the predicted sky brightness for a filter epoch (in mag/arcsec^2 above dark) to be less than $3/3/2/2$ for $g/r/i/z$. For the shallow fields this is loosened to $5/4/2/2$ if $\Delta t_{\rm seq} \geqslant 7$ days, as otherwise the filters being tied together in one observing sequence would result in long gaps *in red filters* owing to the brightness of the Moon. `ObsTac` additionally requires a starting airmass <1.5 per sequence, though this is

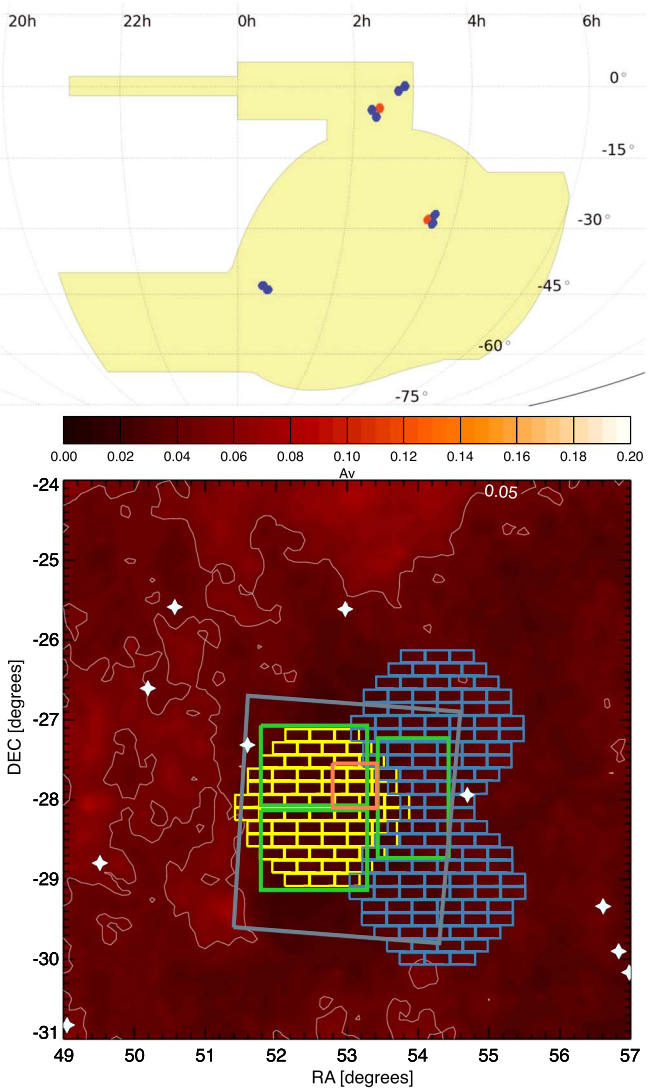

Figure 1. Top: the DES footprint (yellow), with the DES-SN shallow (blue) and deep (red) fields overplotted. A Mollweide equal-area projection is used. Positions of fields are listed in Table 2. **Bottom:** enlarged view of the DES-SN C fields. The shallow fields (C1 and C2) are again in blue and deep C3 is outlined in yellow. These DECam footprints are plotted over a contour plot of Milky Way extinction. Bright stars ($M_V < 8$ mag) are plotted in white. Overplotted are the boundaries of fields observed by SWIRE (gray), VIDEO (green), and CDFS (orange).

loosened at the edges of each season and sometimes before any bright-time shutdown to avoid long observing gaps.

The data quality (DQ) for each exposure is assessed based on an analysis of its output from the difference imaging pipeline (`DiffImg`; Kessler et al. 2015). There are three possibilities for the status of an exposure: Pass, Fail, or Junk. Pass means that minimal acceptable DQ has been achieved and that $\Delta t_{\rm seq}$ should be reset to zero, while Fail means it has not. Specifically, an image fails DQ if the measured point-spread function (PSF), converted to i-band zenith, is $>2\farcs0$, or if the artificial sources of magnitude 20 we insert into our pipeline have a measured signal-to-noise ratio (S/N) of <20 (<80 for the deep fields). Junk means that the pipeline was unable to process the image, either due to instrumental errors or exceedingly poor weather. If an exposure is labeled as Fail or Junk, then it is not considered "accepted," and the clock for retaking the sequence ($\Delta t_{\rm seq}$) is not reset to zero.

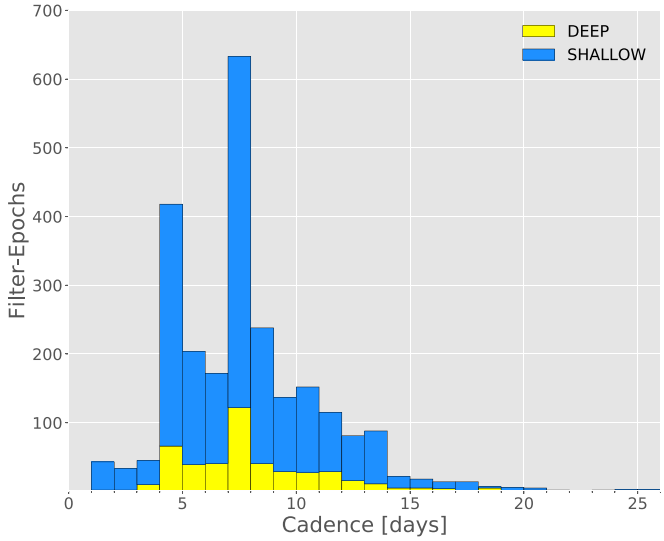

Figure 2. Stacked histogram of the number of days between good-quality data in a single filter epoch over the first three years of the DES-SN program, split between deep (yellow) and shallow (blue) fields. Note the peak at 4 days (when observations can be made owing to adequate seeing), and at 7 days (when observations begin to be forced regardless of the seeing).

2.5. Survey Summary Statistics

The DES-SN program took 6877 exposures totaling 487.69 hours of on-sky time during the first three years of the survey. Data quality was assessed as Pass for 87.7% of the exposure time. The mean number of total (Pass) epochs per field per season was 29.3 (24.6) for each shallow field and 25.6 (22.7) for each deep field. The number of good filter epochs per season varied from 15 to 28, while the total number was in the range 21–32.

The mean duration of the observing season for each DES-SN field was 167 days, with only small variations across the seasons (163/168/170). The observing season per field varied from 153 days (X3r in Y3) to 182 days (C3z in Y2). Typically the southern fields have a longer continuous visibility than the more northerly fields (171 days for SN-C and SN-E; 160 and 164 for SN-S and SN-X, respectively.)

The mean cadence for DES was 7.4 days when considering only good-quality imaging; the cadence was 6.1 days when including all imaging. The shallow fields have a slightly better cadence than the deep fields (7.3 days and 7.8 days, respectively). The shallow fields vary between a cadence of 7.1 days to 7.5 days and in the deep fields—where bands are observed independently—there is no effective difference in cadence (range of 7.7 days to 7.9 days). The median for all of the above quantities is 7 days.

Figure 2 shows a histogram of the cadences for the first three years of DES-SN, split by field depth. Sixty-eight percent of all epochs were taken with a cadence of 4–8 days and 23% were taken with a cadence of 9–13 days. Although observations are given top priority programatically at $\Delta t_{\rm seq} = 7$ days, a number of factors cause a long tail to higher cadences. In particular, there are poor-weather nights, nights DES is off-sky for community time, nights when sky brightness is above the observing threshold, and nights when the time allotted for programmed DES-SN sequences exceeds the time of field visibility.

We note that there are cases where we have a cadence <4 days, seemingly in contradiction with `ObsTac`. There are two

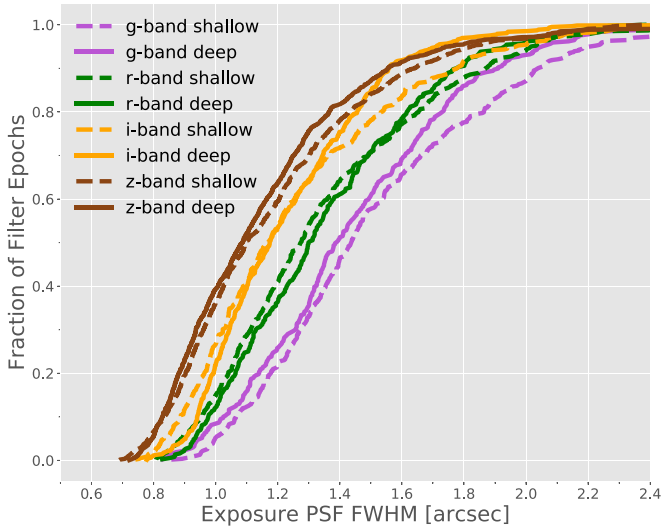

Figure 3. Distribution of observed PSF FWHM (in arcseconds) for each exposure in the first three years of the DES-SN survey.

causes for this. The majority of the short-cadence exposures (79%) come from a shallow field sequence where one filter fails DQ but the others pass; in these cases $\Delta t_{\rm seq}$ is not reset, which can lead to short cadences for some filters. The remaining short-cadence exposures are due to data-processing lags, where DQ was not accessed prior to the next night's observations. We have only 61 filter epochs with a gap in the cadence >15 days, on average 0.5 per filter epoch per season. Fewer than half of these gaps occur between September 15 and January 31. Therefore, most of the large light-curve gaps are at the very beginning (when weather is often poor), or at the very end of the season, when overriding of `ObsTac` was permitted. As the end of the DES-SN season is needed to complete already-discovered SN light curves rather than to search for new SNe, assessment of the overall DES collaboration needs permitted a reduced DES-SN cadence without sacrificing SNe that could potentially be part of a cosmological-analysis sample.

In Figure 3 we show the cumulative distribution function (CDF) for the measured FWHM of the point-spread function (PSF) for each DES-SN exposure, split by band and depth. The measured FWHM is larger for bluer bands, as the atmosphere produces a larger PSF for smaller wavelengths. The median observed FWHM in griz (in arcseconds) is 1.41/1.29/1.17/1.09. As seen in Figure 3, the distributions of FWHM are similar for the deep and shallow fields with the exception of the poorest ∼10% of images in the deep fields, which were taken in significantly better conditions than those in the shallow fields. This is as expected given our observing algorithm. We note that for real-time scheduling decisions, `ObsTac` does not use the measured FWHM but rather it uses the *i*-band zenith PSF to prioritize observations. As a consequence, the median *i*-band zenith PSF is consistent across all bands, as expected.

In Figure 4 we plot the distribution of limiting magnitude of each filter epoch, split by band. The median depth across all bands is very similar, which was the intended outcome of our chosen exposure times. Despite our usage of the term "shallow," these fields have per-exposure depths of ∼23.5 mag, deeper than SDSS (Sako et al. 2018) and equal to or slightly deeper than the Pan-STARRS Medium-Deep Survey (Rest et al. 2014). The

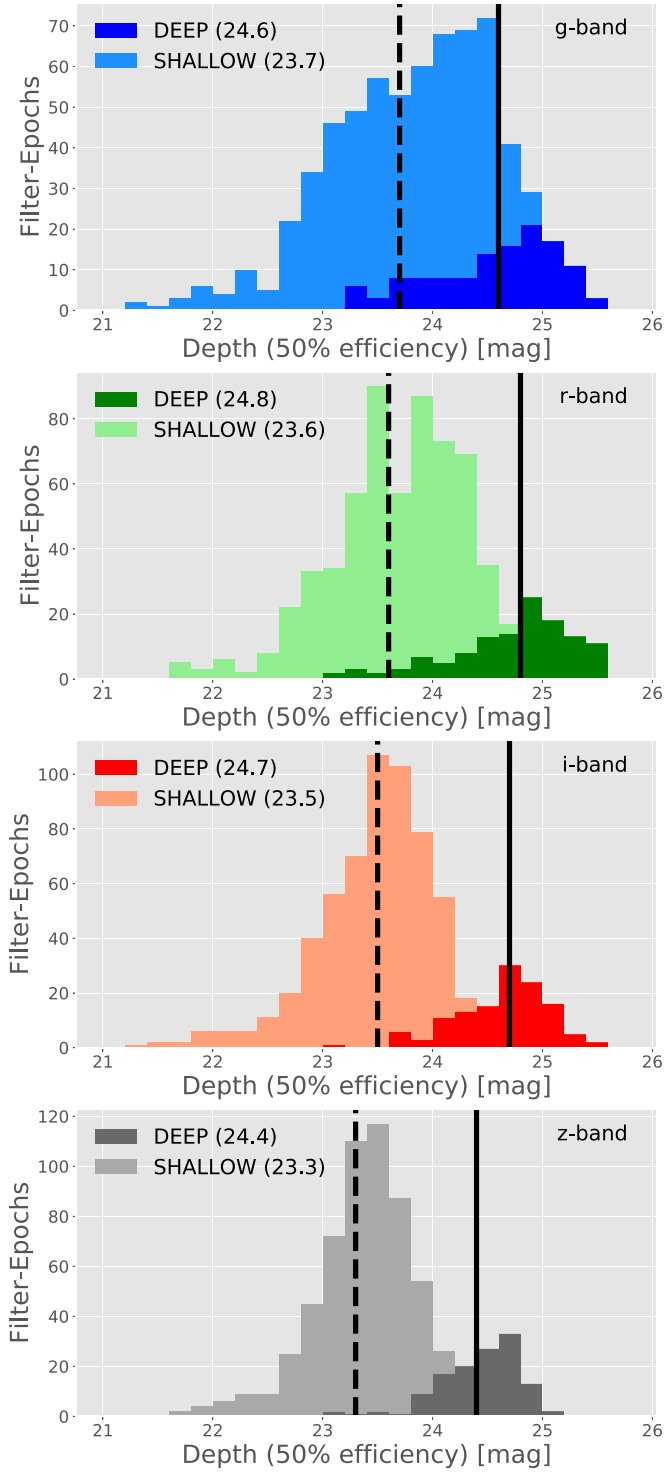

Figure 4. Depth of the DES filter epochs in the first three seasons of the survey, split by deep and shallow fields. The median depth in the deep and shallow fields is shown by solid and dashed lines, respectively.

larger variation in bluer bands is an effect of observing across a large variety of sky brightness conditions.

3. Transient Identification

In order to rapidly detect transient candidates and trace the evolution of previously discovered events, DES-SN data was processed nightly at the National Center for Supercomputing

Applications (NCSA[83]) in Urbana-Champaign, IL. Next, we briefly describe these steps and how they have evolved during the survey. We end this section with statistics for detections over the first three seasons of DES-SN.

3.1. Image Processing, Difference Imaging, and AutoScan

DES observations are transferred from CTIO to NCSA at the end of each exposure, where they are bias-subtracted, flat-fielded, masked for bad pixels, and corrected for crosstalk and nonlinearity by the DES Data Management team (DESDM). Saturated stars and their bleed trails, cosmic rays, and satellites are masked out, and the sky background is measured and subtracted from the image as described in Morganson et al. (2018).

Transients are identified from these images via the DES-SN Difference Imaging Pipeline `DiffImg` (Kessler et al. 2015). All exposures in a given filter epoch are coadded to form a single "search image." Source extraction is performed on both search and "reference images" (created by coadding images taken in good conditions during previous DES observing seasons) to determine a common astrometric solution. The images are PSF-matched and the reference is subtracted from the search image to create a "difference image" from which sources are extracted. Every source detected by `DiffImg` on every filter epoch is classified as an "object," and is saved in a database.

Each detected object is evaluated by a supervised machine-learning algorithm (`autoScan`; Goldstein et al. 2015), derived from features computed directly from the difference, search, and reference images. `autoScan` determines whether each source is likely to be a real astronomical point source or an artifact of the reduction pipeline (unmasked artifact, subtraction error, etc.). `autoScan` assigns a score (0–1) to each object, where a higher score indicates a higher likelihood of the object being a non-artifact. An object with an `autoScan` score $\geqslant$0.5 is labeled an "ml_object" to specify that it has passed machine learning and is most likely a detection of a real astrophysical transient.

3.2. Candidates and Transients

The presence of multiple spatially and temporally coincident "objects" triggers the creation of a "candidate." Two objects detected in different images within 1″ of the same position, both of which have an `autoScan` score $\geqslant$0.3 (intended to minimize the number of real transients discarded), in any combination of filters and detected less than 30 days apart receive a unique SuperNova IDentification number, or SNID. PSF-fitted photometry (i.e., "forced photometry") is measured on all previous images at the candidate's position and updated with each subsequent observation (Kessler et al. 2015). SNIDs are provided as unique IDs in all DES-SN data-release products.

To remove slow-moving asteroids and lower the contamination rate, a "transient" (hereafter *transient*) is defined as a candidate consisting of at least two ml_objects detected on more than one night. All *transients* are given unique names in the format "DESXXYYzzzz" based on their location and time of discovery. "XX" represents the last two digits of the year in which that observing season began (13, 14, and 15 for DES Y1, Y2, and Y3, respectively) while "YY" is filled by the DES-SN field in which the *transient* was first discovered. "zzzz" is a unique alphabetical identifier within the season that ascends as the season progresses (a, ..., z, aa, ..., zz, etc.). Each *transient* is matched to a likely host (Section 3.3), and its light curve is compared to template SN light curves (Section 3.4) to prioritize the event for spectroscopic follow-up observations.

To further prioritize SNe over spurious detections and slowly evolving astrophysical transients, such as active galactic nuclei (AGNs), we define a "transient_status" flag to remove the most commonly found cases of artifacts that pass our simple *transient* criteria. There are four indicators of an artifact for which we evaluate: (i) pixel correlation (repeated detections on a single pixel, column, or row), (ii) band multiplicity (nonphysical fraction of all detections occurring in single band), (iii) large temporal separation between detections (Δt between ml_objects), and (iv) large quantity of poor subtractions (indicating multiple good ml_objects by chance). For each *transient*, these criteria are evaluated for each season separately. Only objects with a valid transient_status flag in just one observing season are considered as possible targets for spectroscopic follow-up observations.

3.3. Host Galaxies

Host-galaxy matching for the real-time DES-SN survey used the DES SVA1-GOLD galaxy catalog, created from DES Science Verification data and thus free of contaminating SN light. These catalogs are complete to $r \approx 24.4$ mag ($r \approx 25.5$ mag in the deep fields). Photometric redshifts are estimated for all hosts based on a neural network as described in Sánchez et al. (2014).

Host galaxies are assigned to candidates via the directional light radius method (DLR; Sullivan et al. 2006). The DLR method uses the distance between the candidate and the galaxy in normalized units of the light profile, evaluated considering the shape of the galaxy, projected in the direction of the transient ($d_{\rm DLR}$) to identify the likely host. To identify the host galaxy of each *transient*, DLR is computed for all galaxies within a 15″ radius, and the closest galaxy in this dimensionless measure is assigned as the likely host, provided $d_{\rm DLR} \leqslant 4$ (Gupta et al. 2016). If no galaxy satisfies this criterion, the candidate is considered to be hostless.

3.4. Photometric Classification

To prioritize candidates for follow-up spectroscopy we use the Photometric Supernova IDentification software (`PSNID`; Sako et al. 2011). `PSNID` compares the light curve of each candidate to a grid of templates of the most common SN subtypes (SNe Ia, Type II SNe, and Type Ib/c SNe), measuring the best-fit parameters or template for each of the models to the data. The probability that the model describes the data, `FITPROB_SNXX`, is computed, and used to determine the Bayesian probability of the candidate being a particular subtype: `PBAYES_SNXX`. As part of DES-SN real-time survey operations, `PSNID` was run with each new epoch of photometry, both with and without a prior on redshift (taken to be the photo-z of the host) to shape our spectroscopic SN follow-up program.

[83] http://www.ncsa.illinois.edu

Table 3
DES-SN Detection Statistics

Type	Total	Y1	Y2	Y3	Deep[a]	Shallow[a]
Objects[b]	4.88 M	1.63 M	1.66 M	1.59 M	265 K	137 K
ML Objects[c]	1.21 M	421 k	389 k	397 k	52,623	37,139
Candidates[d]	46.0 k	18,555	13,586	13,809	1099	1640
Transients[e]	17,209	6404	5521	5284	731	534
SSTs[f]	11,995	4259	4192	3544	592	352

Notes.
[a] Mean number per field type, per season.
[b] Detection in a single filter epoch by `DiffImg` as defined in Section 3.1.
[c] Objects with (`autoScan` score $\geqslant$0.5) as defined in Section 3.1.
[d] Spatially coincident detections as defined in Section 3.2.
[e] Candidates consisting of ML Objects on multiple epochs as defined in Section 3.1.
[f] Transients with "transient_status" >0 in one season only. See Section 3.2 for details.

3.5. Candidates Detected

Table 3 presents statistics describing the number of objects, candidates, and *transients* found in each of the first three seasons of DES-SN. From three seasons of DES-SN, we discovered 11,995 single-season *transients* (SSTs), an average of 24 per night.

The differences in statistics between seasons are quite small, with $\mathcal{O}(10\%)$ variation among seasons. Candidates observed across multiple seasons (e.g., AGNs) are attributed to the first season in which they appear. As such, Y1 has a much higher number of candidates than the other seasons, but a consistent number of SSTs. Splitting by field, the DES-S and DES-X shallow fields, with close proximity to the ecliptic, have 220% more candidates per field than the more southerly shallow fields (C1, C2, E1, and E2) but the same number of *transients* to within 5%, highlighting the need for multi-epoch detection prior to spectroscopic classification.

4. Spectroscopy

In this section we give a full overview of the SN spectroscopy program for the first three seasons of DES-SN. Section 4.1 describes the strategy used to select SN candidates for live follow-up spectroscopy, while Section 4.2 describes the tools used to facilitate this task. With our strategy and requirements in place, Section 4.3 details the spectroscopic resources available to DES-SN, along with a brief description of the reduction techniques used. The methodology used to classify individual spectra is discussed in Section 4.4 with results as a function of observatory and redshift given in Section 4.5. A full observing log of all spectroscopic data taken by DES-SN can be found in Appendix A1, with all classifications obtained listed in Appendix A2.

4.1. Follow-up Strategy and Target Selection

With the primary cosmological analysis of DES-SN driven by photometrically classified SNe Ia, the prioritization of objects for follow-up spectroscopy is no longer solely driven by the need to place events on a Hubble diagram. The DES-SN spectroscopic sample is a complementary probe used to constrain systematic uncertainties and biases in the photometric sample.

For DES-SN, the spectroscopic sample constitutes a truth sample for training photometric classification in DES. It is needed to evaluate the impact that spectroscopic properties have on light-curve properties (e.g., Foley et al. 2011) and, with a known correlation between SN Ia properties and host-galaxy properties (Sullivan et al. 2010; Kelly et al. 2010; Smith et al. 2012), to alleviate potential biases caused by the loss of SNe in low-luminosity galaxies that will be missed by our spectroscopic follow-up program of SN host galaxies. Most crucially, though, SN spectroscopy allows for an independent cosmological analysis, testing the quality of our data and our analysis techniques. With limited spectroscopic resources available (Table 4), here we describe the four modes of our live spectroscopy program and how they were implemented in the first three years of DES-SN.

4.1.1. A Magnitude-limited Sample

A magnitude-limited sample is a useful component for a spectroscopic SN survey in that it creates an easily quantifiable selection function of all SNe. Spectroscopically confirming all SSTs without bias, this sample is used for testing and validation of photometric classification routines.

The primary source of observations for this program was the OzDES program (Yuan et al. 2015; Childress et al. 2017; Lidman et al. 2020). On any given OzDES observing night, all active SSTs with $r < 22.7$ or $i < 22.7$ mag in the field being observed have a fiber placed on them. These observations were supplemented by those from other observatories—primarily the Southern African Large Telescope (SALT) and MMT—to obtain classifications of SSTs not obtained at the AAT owing to weather, observing cadence, or other classification inefficiencies. The goal for completeness in this campaign was all SSTs brighter than $r = 21.5$ mag, though as we will demonstrate later this goal was not achieved.

4.1.2. SNe Ia in Faint Hosts

Since the inclusion of a SN in the photometric cosmology analysis requires a spectroscopic redshift, all SNe occurring in galaxies too faint for our OzDES host-galaxy spectroscopy campaign ($r > 24$ mag; see Lidman et al. 2020 for details) would be excluded from our cosmology sample. This creates a selection bias against SNe Ia as a function of both decreasing host-galaxy mass as well as increasing redshift. To characterize this bias we carried out a follow-up program for spectroscopically classifying SNe Ia in faint host galaxies, ensuring that these SNe Ia can be retained in our final analysis. The redshift information obtained from the spectrum can be used alone or in conjunction with the spectroscopic classification.

Table 4
DES-SN Spectroscopy Program

Observatory	PI	Mode	Instrument	Wavelength (nm)	Allocation[a]	Targeting strategy[b]	Season	Spectra[c]
AAT	C. Lidman[d]	Classical	2dF/AAOmega	380–880	48n	mag lim; non-Ia	Y1,Y2,Y3	1032
AAT	C. Smith[d]	Classical	2dF/AAOmega	380–880	2n	mag lim; non-Ia	Y1	7
Gemini-S	R. Foley[d]	Queue	GMOS	520–990	18 h	representative	Y1	2
Gemini-N/S	R. Foley	Queue	GMOS	520–990	39.6 h	representative	Y3	25
Gemini-S	L. Galbany	Queue	GMOS	520–990	10 h	faint host; non-Ia	Y3	4
GTC	F. Castander	Queue	OSIRIS	480–920	54.6 h	non-Ia	Y1,Y2,Y3	19
Keck	A. Filippenko[d]	Classical	DEIMOS	455–960	4n	representative	Y1,Y2,Y3	7
		Classical	LRIS	340–1025	11.5n + 26 h	representative	Y1,Y2,Y3	19
Magellan	R. Kirshner	Classical	LDSS3	425–1000	2n	representative	Y2,Y3	23
		Classical	IMACS	390–1000	8n	representative	Y2,Y3	33
Magellan	S. González-Gaitán	Classical	LDSS3	425–1000	4n	faint host; non-Ia	Y3	23
Magellan	D. Scolnic	Classical	LDSS3	425–1000	1n	representative	Y3	7
MMT	R. Kirshner	Classical	BCS	330–850	7n	mag lim	Y2,Y3	30
SALT	M. Smith	Queue	RSS	385–820	41.6 h	mag lim	Y1,Y2	21
SALT	E. Kasai	Queue	RSS	385–820	37.5 h	mag lim	Y3	31
VLT	M. Sullivan	Classical	X-Shooter	300–2480	14.1n	faint host	Y2,Y3	89
VLT	M. Sullivan	Queue	X-Shooter	300–2480	13 h	non-Ia	Y1,Y3	8
Miscellaneous[e]	…	…	…	…	…	…	…	5
Total					101.6n + 233.3 h			1385

Notes. Program IDs for the spectroscopic campaigns listed here can be found in the acknowledgements.
[a] Hours are used for queue-scheduled time, nights for classical time.
[b] Primary selection criteria used as described in Section 4.1.
[c] Number of spectra of DES-SN candidates obtained.
[d] Program includes spectroscopy of live DES-SN targets, but is not the primary purpose of the program.
[e] Spectroscopic observations, obtained from other facilities, including SOAR, LICK/Shane, PESSTO/NTT and the KISS Survey. These are primarily serendipitous observations of bright DES-SN transients observed by other surveys.

SN Ia candidates for this program are selected based on their early-time light curve, fit with PSNID, and prioritized based on the apparent faintness of their host galaxy. There is overlap between this program and the magnitude-limited one, as a bright candidate can also be hostless. The faint hosts program (which targets SNe in faint galaxies, not the galaxies themselves) had dedicated observing time at the Very Large Telescope (VLT) and the Gran Telescopio Canarias (GTC), with additional data taken using Keck and Magellan.

4.1.3. A Representative Sample of SNe Ia

The last of the three live SN Ia follow-up programs in DES-SN is designed to obtain a representative sample: a spectroscopically confirmed sample of SNe Ia that evenly samples the redshift distribution of SNe in the final photometrically classified analysis. This sample allows us to test for environmental dependence and evolution of spectroscopic properties with redshift. With this information missing from a photometric analysis, by quantifying this effect and optimizing cuts to alleviate its impact, we can ensure that the cosmological constraints obtained from our photometrically selected sample are unbiased.

For this follow-up program, we first determine likely SN Ia candidates using PSNID fits. The other follow-up programs independently fill portions of this parameter space, e.g., low-redshift SNe for the magnitude-limited sample and (preferentially) high-redshift SNe for the faint host sample. As a result, the representative program primarily observes SNe Ia at redshifts $0.3 < z < 0.7$, and is biased toward higher-mass hosts at high redshift, areas that are missed by our other follow-up programs. Dedicated observing programs at Gemini and Magellan comprise the majority of this sample, though data for this was collected at Keck and MMT as well.

4.1.4. Non-Ia Supernovae

DES is a cosmology survey, and thus DES-SN has been designed to discover, measure, and confirm SNe Ia. But as a deep and wide transient survey, there are many other interesting types of transients that can be found in the data. We briefly note here three additional classes of transients for which we have made a concerted effort to obtain follow-up spectroscopy: superluminous SNe (SLSNe), rapidly evolving transients (RETs), and Type II SNe (SNe II).

These programs are much smaller than our SN Ia program, with the only follow-up time specifically allocated for such observations coming from the VLT (SLSNe; RETs), GTC (SLSNe), Magellan (SN II), and Gemini (SN II). Despite limited spectroscopic time, non-Ia events classified by DES-SN have been discussed widely (Papadopoulos et al. 2015; Smith et al. 2016; Pan et al. 2017; Pursiainen et al. 2018; Smith et al. 2018; Angus et al. 2019; de Jaeger et al. 2020).

4.2. Facilitating Follow-up Spectroscopy

To successfully carry out our multiple spectroscopic observing programs across a globally distributed collection of telescopes requires real-time coordination and centralized data storage. For this purpose we developed a tracking database and web application called ATC,[84] hosted at the National Energy Research Scientific Computing Center (NERSC).

[84] ATC: All Transients Considered; https://portal-auth.nersc.gov/atc2/web/.

Table 5
DES-SN Spectroscopic Statistics

Telescope	Spec Observations	Spec Ia[a]	Spec Ib/c[a]	Spec II[a]	Spec SLSN[a]	Spec TDE[a]
AAT	1039 of 547 SN	78 (188 of 106)	1 (9 of 2)	14 (45 of 19)	0 (2 of 1)	0 (-)
Gemini-N/S	31 of 29 SN	21 (21 of 21)	2 (2 of 2)	0 (-)	1 (3 of 1)	0 (-)
GTC	19 of 18 SN	10 (11 of 11)	0 (-)	0 (-)	5 (6 of 5)	0 (1 of 1)
Keck	26 of 23 SN	11 (11 of 11)	0 (-)	2 (2 of 2)	1 (4 of 3)	0 (1 of 1)
Magellan	86 of 86 SN	49 (56 of 56)	1 (1 of 1)	6 (6 of 6)	0 (-)	1 (1 of 1)
MMT	30 of 27 SN	12 (12 of 12)	0 (-)	0 (1 of 1)	1 (1 of 1)	0 (-)
SALT	52 of 43 SN	18 (25 of 24)	4 (4 of 4)	2 (2 of 2)	0 (-)	0 (-)
VLT	97 of 92 SN	49 (50 of 50)	1 (1 of 1)	10 (11 of 10)	4 (7 of 5)	0 (-)
Others (SOAR & LICK)	3 of 3 SN	1 (1 of 1)	0 (-)	1 (1 of 1)	0 (-)	0 (1 of 1)
External (PESSTO & KISS)	2 of 2 SN	2 (2 of 2)	0 (-)	0 (-)	0 (-)	0 (-)
Total	1386 of 869 SN	251 (377)	9 (17)	35 (68)	12 (23)	1 (4)

Note.
[a] Spectroscopic discoveries. Total number of spectra taken and unique transients observed is given in brackets.

After discovery of each DES transient, a "portfolio" on ATC is created. Information including coordinates, photometry, discovery date, and host-galaxy association are propagated to ATC upon creation, with each new photometric data point and light-curve fit pushed in real time. Using a tagging system to indicate to observers which transients should be observed, when, and from where, follow-up spectroscopy is coordinated and scheduled through ATC. With utilities to produce finder charts, store and visualise reduced spectra, and track candidates of interest, all of the DES-SN follow-up spectroscopy, which we detail in the following section, was dependent on the ATC.

4.3. Spectroscopic Observations and Reductions

Here we describe the observing campaigns undertaken by DES. In Table 4 we list the main details of the spectroscopic programs for which DES SN Ia targets were observed including the targeting strategy used for each facility and the number of candidates targeted under each program. The number of unique transients targeted and classified by each facility is listed in Table 5.

Appendix A1 presents our observation log of spectra taken of DES transients. For each observation we list the DES transient name, the telescope or instrument, the MJD and UT date of the observation, the magnitude of the transient at the time of observation, and the percent increase of the flux from the transient over the background flux. All long-slit observations were carried out at the parallactic angle (Filippenko 1982). We note that Table 4 lists the total allocated time, not on-sky time, and that repeated observations of the same target are counted in the observation log. As a result, classification efficiency cannot be directly related from the number of confirmed events. The algorithm used to classify individual spectra is discussed in Section 4.4, with the results given in Table 5 and Appendix A2.

Spectroscopic reductions were performed by the individual observing teams using pipelines developed for each facility/instrument, usually based on standard IRAF routines[85] with the exception of OzDES which used a modified version of the 2dfdr[3] pipeline (Croom et al. 2004). Raw spectra were bias/overscan-subtracted, flux- and wavelength-calibrated, and rectified prior to an extraction of the SN spectra. For higher-redshift targets embedded in their hosts, modest spatial-width apertures were used when extracting the SN spectra to minimize host contamination.

4.4. Spectroscopic Classification

To classify our reduced spectra we use the publicly available `SNID` (SuperNova IDentification; v5.0; Blondin & Tonry 2007) and `superfit` (v3.5; Howell et al. 2005) software packages with updated template libraries based on the spectroscopic catalogs of Silverman et al. (2012), Liu et al. (2016), Modjaz et al. (2016), Gutiérrez et al. (2017), Quimby et al. (2018), and Williamson et al. (2019). These approaches use cross-correlation techniques (`SNID`) and chi-squared minimization (`superfit`) to produce, for a given spectrum, a rank-ordered list of matches from a spectral library of SNe, galaxies, or any other variable objects. These codes also allow for external information, such as redshift and phase, to be included in the fit. Where available, all fits were performed using the spectroscopic redshift obtained either from galaxy emission lines in the spectrum itself or from literature data. Owing to its inclusion of galaxy contamination when fitting the observed spectrum, `superfit` was used as the primary classification tool for most events.

Classifications were determined via visual inspection of the resulting rank-ordered fits by a subset of coauthors, and were based on consensus of the best-fit templates. For spectral classification, we consider the following classes of events "SNIa," "SNIbc," "SNII," "SLSN-I," "TDE," "AGN," "M-star," "galaxy" and "uncertain." Spectra with obvious signal, but no obvious transient light are classified as "galaxy," while those with some signal from a transient, but no convincing template matches are classified as "uncertain." All transient classifications are determined by matches returned by either `SNID` or `Superfit` with the exception of the solitary spectroscopically confirmed tidal disruption event (TDE), which was classified by visual comparison with known TDE spectra. For SNe Ia classifications we do not attempt to subcategorize events as peculiar subtypes (e.g., SN 1991T, SN 1991bg, SN Iax) owing to a combination of the features that characterize these classes (e.g., Si II λ6150) being routinely redshifted outside of the maximum wavelength observed and

[85] Image Reduction and Analysis Facility: IRAF was distributed by the National Science Foundation's (NSF's) National Optical-Infrared Astronomy Research Laboratory, which was managed by the Association of Universities for Research in Astronomy (AURA) under a cooperative agreement with the NSF.

the relatively low S/N of many spectra, which are primarily used to distinguish SNe Ia from other types.

For a definitive classification to be claimed, both the approximate phase of the SN, as determined from the light-curve evolution, and the spectroscopic redshift (if available) must match the entire list of best-fit templates returned by SNID or superfit. If no spectroscopic redshift from the host galaxy is available, then the SN redshift can be fit as well, and a definitive classification can be claimed if the phase, type, and redshift are robustly determined by the fitting software. For SNe Ia where the characteristic feature that defines this class, Si II λ6150 is routinely redshifted outside of the maximum wavelength observed (e.g., $z = 0.4$ for AAOmega), a spectral classification is claimed only if the presence of Si II λ4100 can be inferred either directly or in combination with subtraction of galaxy light in superfit to distinguish these events from SNe Ic.

Where a classification is highly probable but with some degree of uncertainty, we use the following classifications: "SNIa?," "SNIbc?," "SNII?," and "SLSN-I?." These classifications are used in two cases. The first is when there is no independent host-galaxy prior on the redshift and a small fraction of viable fits exist with a redshift and/or type that differs from the primary classification. The second is where a spectrum is a good fit to templates over only one half of the spectrum for plausible reasons: a low-S/N spectrum, poor sky subtraction, or host-galaxy contamination (primarily in the red portion of the spectrum, as the SN is typically brightest in the blue). The phase is still required to match the light curve in all cases. Spectra where SNID and superfit return differing best-fit classifications are classified as "uncertain," with the exception of spectra where host-galaxy light is known a priori to dominate over transient light. In these cases, accounting for ~10% of all classifications, the superfit classification, which simultaneously fits for both transient and galaxy is used as the primary classification tool.

Figure 5 shows a range of spectroscopic classifications from DES-SN with their best-fit template models overplotted.

4.5. Spectroscopic Results

Table 5 presents the results of the spectroscopic program from the first three seasons of the DES-SN program. Of 707 transients spectroscopically targeted, we have classified 307 SNe and 1 TDE over a redshift range of $0.017 < z < 1.86$ and a dynamic range of >1000 in peak observed flux. Table 6 splits our full sample by spectroscopic type. Combining certain and likely classifications, we have identified 251 spectroscopic SNe Ia, 35 SNe II (including IIn and IIb), 12 SLSNe, and 9 SNe Ib/Ic. Spectroscopic classifications obtained by DES-SN are listed in Appendix A2.

In Figure 6 we show the redshift distribution of the SNe Ia classified by our program, color-coded by the telescope that provided the classification. The observing program that drives the follow-up for each telescope can be seen in the redshift range of classified SNe Ia in the figure. VLT (faint hosts) dominates at high-z, while the AAT and SALT (magnitude-limited) fill out medium and low redshifts. Magellan and Gemini extend from mid- to high redshift owing to a mixture of magnitude-limited and representative programs.

In Figure 7 we show the apparent magnitude distribution of transients targeted, and classified, as a function of telescope, where the magnitude is taken from the DES epoch immediately preceding the spectroscopic observation. Here we include *all* classifiable spectra as successes, including where the transient targeted has previously been spectroscopically confirmed. Note that while OzDES obtained nearly three times as many spectra as all the single-slit programs combined, the classification efficiency for AAT (~25%) was far below that of the single-slit follow-up (>70%).

We show in Figure 8 the classified versus unclassified spectra obtained at VLT, plotted as a function of apparent magnitude, percent increase over background, and S/N (indicated by the size of the points). To compute the S/N for each spectrum we split the region $5000 < \lambda(\text{Å}) < 9000$ into 200 Å sections, and determine the rms about the best-fit line in each section. The S/N for the spectrum is then the average over all sections of the mean flux over rms per section. The linear fitting accounts for the fact that an SN spectrum has broad lines and therefore the simple rms cannot be used as an indicator of uncertainty alone. As expected, we find that the non-classified spectra tend to lie in the regime of low S/N and/or faint objects. By design there are very few transients observed with this program that are not significantly above the background. As a result, our classification efficiency with VLT is high.

The number of spectroscopic classifications increased dramatically as the DES survey progressed. While the number of AAT nights increased modestly (from 10 to 12 to 16), the number of DES-SN spectra obtained from all other observatories over the first three seasons rose from 27 to 127 to 203. This expansion of resources resulted in 24/75/152 spectroscopically classified SNe Ia and 34/95/179 spectroscopically classified transients in DES Y1/Y2/Y3, respectively. We note that the efficiency of the survey pipeline itself also improved through the seasons; both the speed at which DES data were processed and the quality of artifact rejection increased dramatically from Y1 to Y3. These improvements also contributed to the year-on-year increase in classified SNe Ia.

5. Selection Function

A key input to the DES-SN3YR cosmology analysis is the spectroscopic selection function ($E_{\rm spec}$): the function that describes how the spectroscopically confirmed SN Ia sample relates to the broader set of photometric candidates that could have been observed. Understanding and modeling $E_{\rm spec}$ is critical as it is used through simulations to determine the bias corrections applied to each observed event. Modeling all the features and selection criteria that shape $E_{\rm spec}$ is exceptionally challenging: these range from real-time changes in observing conditions at follow-up telescopes to human prioritization of candidates when observing, and, with most follow-up resources primarily available in dark time, variation of our follow-up capabilities across the lunar cycle. With a large number of variables and human intervention in the decision-making process, rather than attempting to model $E_{\rm spec}$ from first principles, we instead determine an empirical *effective* $E_{\rm spec}$ for SNe Ia in DES.

This section is as follows. In Section 5.1 we derive $E_{\rm spec}$ from DES-SN data alone. In Section 5.2 we independently derive $E_{\rm spec}$ using a forward-modeling approach, as discussed in Kessler et al. (2019), and used in the nominal DES-SN3YR cosmology analysis Brout et al. (2019b), and use both estimates to simulate DES-SN, which we then compare to the DES-SN sample in Section 5.3. In Section 5.4 we show how the different estimates of $E_{\rm spec}$ affect the distance-modulus bias

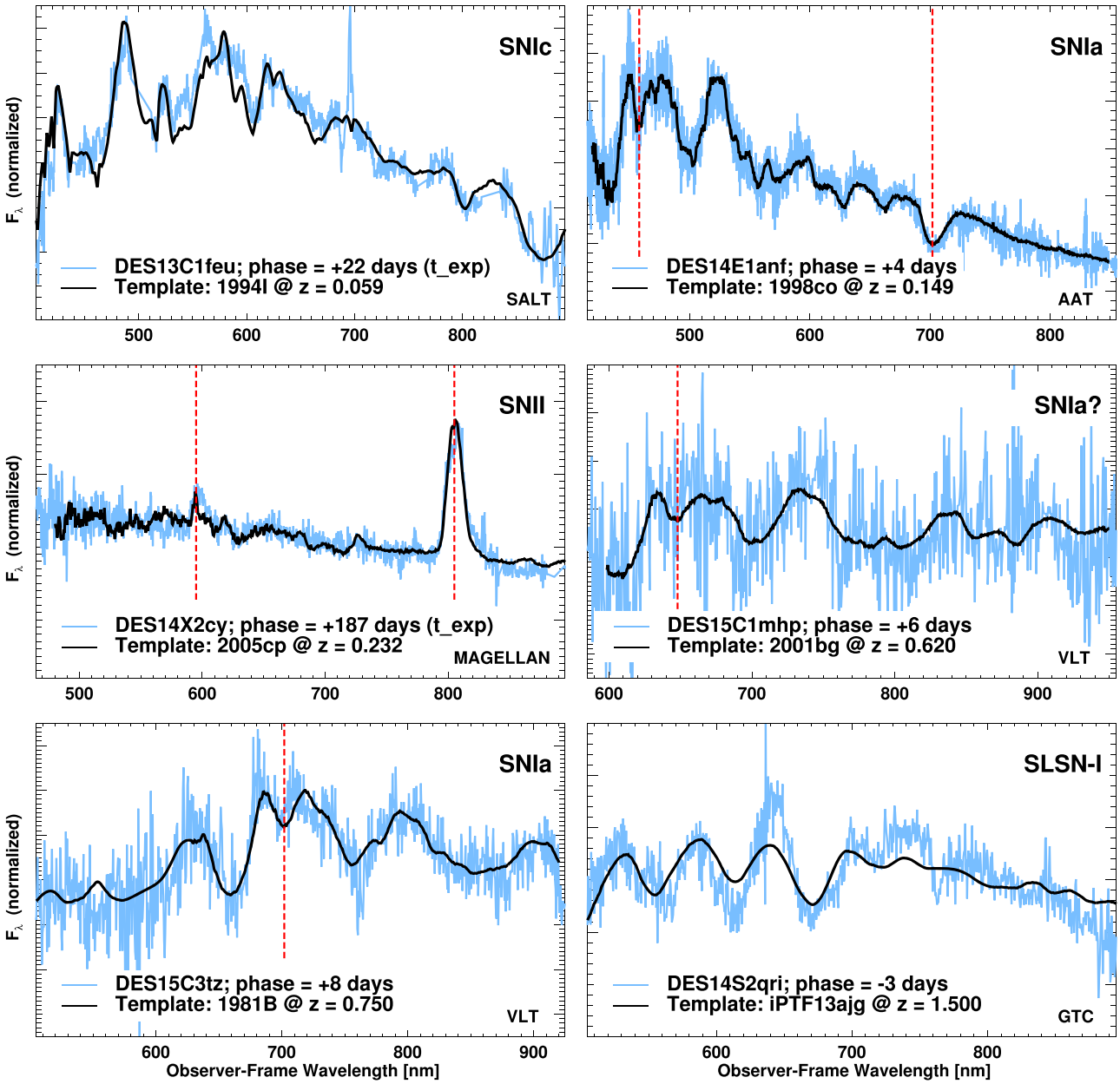

Figure 5. Example spectral classifications from the DES-SN3YR data set. Spectra are plotted in blue with the best-fit SN template overplotted in black. Fits are derived using `superfit`. Prominent spectral features used to classify each object (λ6150, λ4100 for SNe Ia; λ4861, λ6563 for SNe II) are highlighted with vertical red dashed lines. The classification of each object and facility used is highlighted in each panel.

Table 6
DES Classification Summary

Type	Classifications
SNIa	225
SNIa?	26
SNII	24
SNII?	9
SNIIn?	1
SNIIb?	1
SNIbc	5
SNIc	4
SLSN-I	11
SLSN-I?	1
TDE	1

correction for our spectroscopic SN Ia sample and discuss the implications for the cosmological parameters determined for the DES-SN3YR sample. The results presented here do not supersede the results presented in Brout et al. (2019b) and Kessler et al. (2019), and do not impact the associated systematic uncertainty of the DES-SN3YR cosmological analysis by Dark Energy Survey Collaboration et al. (2019b).

5.1. Deriving E_{spec} Directly from DES-SN Data

$E_{\rm spec}$ is the fraction of cosmologically useful SNe Ia identified as candidates by DES-SN that are subsequently spectroscopically classified. Thus, the denominator of $E_{\rm spec}$ should be the subset of SSTs (Section 3.2) detected by DES that were real SNe Ia. Since we do not know the true

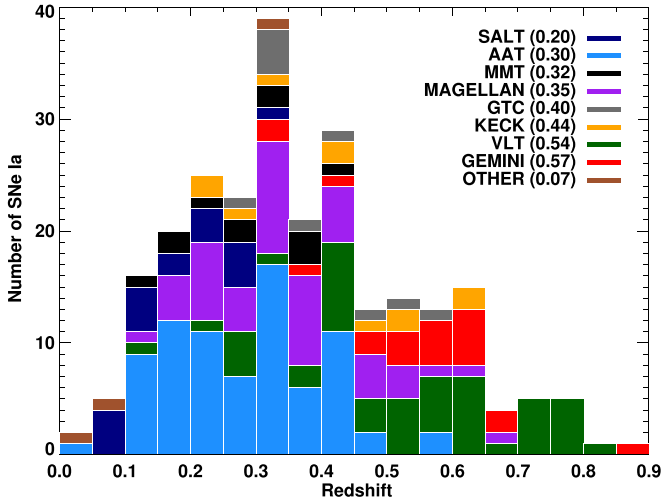

Figure 6. Redshift histogram of all 251 spectroscopically confirmed SNe Ia in the first three seasons of DES ($\Delta z = 0.05$). The histogram is split by discovery observatory, with the median redshift of the SNe Ia classified by each telescope indicated in the legend.

classification of all SSTs from DES, we determine the likely number of SNe Ia based on the results of photometrically classifying our full three-year data sample. In contrast to the real-time survey where decisions were based on rising incomplete light curves, here, for consistency and increased accuracy, we use the full light curves for every object. We define $E_{\rm spec}$ as a function of the peak magnitude of the transient in the observer-frame i band (m_i), which was used to prioritize most spectroscopic follow-up decisions. Thus,

$$E_{\rm spec}(m_i) = \frac{N_{\rm SpecIa}(m_i)}{N_{\rm PhotIa}(m_i)}. \quad (1)$$

To determine $N_{\rm PhotIa}$, we first select all 12,015 SSTs from the first three seasons of DES. To remove spurious artifacts from the data, we require each transient to have peak S/N $\geqslant 5$ in at least two bands. We then fit the full light curves with PSNID (Section 3.4), using both the SN Ia light-curve models and core-collapse SN (CCSN) templates from Sako et al. (2011). To ensure that our results are unbiased with respect to whether a transient has been matched to a host or not or has independently obtained a spectroscopic redshift, we assume a flat prior on redshift in the light-curve fit. To determine a sample of all likely SNe Ia, we use cut thresholds defined by Sako et al. (2011, 2018) and select events with a chi-squared probability relative to the SN Ia model, FITPROB_SNIa $\geqslant 0.01$ and SN Ia Bayesian probability, PBAYES_SNIa $\geqslant 0.9$. We exclude at most two filter epochs of photometry with $\Delta\chi^2 \geqslant 10$ from the fitting, guarding against outliers from sub-optimal real-time photometric processing.

We next restrict this sample of likely SNe Ia to those which are *cosmologically useful*. We measure the best-fit light-curve parameters using the Guy10_UV2IR version of the SALT2 model (Guy et al. 2010) in the "SuperNova ANAlysis" (SNANA) software package (Kessler et al. 2009). This model is defined over a wider wavelength range than the B14-JLA model (Betoule et al. 2014), providing more complete coverage of the DES filters over a wide redshift range. This allows us to estimate "'SN only" photometric redshifts across $0.0 < z < 1.2$, and to estimate peak fit rest-frame i-band magnitudes for all SNe Ia. To ensure that all candidates are treated equally independently of whether they were spectroscopically targeted, we use a flat prior on the redshift for all candidate SNe Ia. To remove likely CCSN events and failed fits, we only consider events with $-4 < x_1 < 4$ and $-1 < c < 1$. While these cuts are less stringent than those used to define a cosmological sample, they ensure that all spectroscopically confirmed events are retained. Our final sample comprising $N_{\rm PhotIa}$ consists of 2634 photometrically classified SNe Ia.

For the spectroscopic sample, we similarly fit each of the 251 spectroscopically classified SNe Ia using the "Scene Modeling Photometry" (SMP; Brout et al. 2019a) used in the DES-SN3YR cosmology analysis (Brout et al. 2019b) and consistently enforce $-4 < x_1 < 4$ and $-1 < c < 1$.

To estimate $E_{\rm spec}$, we bin both our photometric and spectroscopic SN Ia samples by peak i-band magnitude as measured from the best-fit SALT2 model, and divide $N_{\rm SpecIa}$ by $N_{\rm PhotIa}$ (Figure 9). This represents the efficiency of obtaining a spectroscopic classification for a transient of a given magnitude based on data alone. Our derived spectroscopic selection function, $E_{\rm spec}$, is given in Table 7.

To normalize $E_{\rm spec}$ we set the efficiency equal to 1 (i.e., 100% classification rate), for objects with $m_i \leqslant 20.3$. While there are 34 SNe Ia (1.3% of the total photometric sample) brighter than this limit which have not been confirmed, these are unconfirmed due to operational issues (lack of telescope time or processing problems), and as such $E_{\rm spec}$ is not a simple function of m_i below this limit.

To determine the statistical uncertainty on $E_{\rm spec}$, we follow the method adopted by Frohmaier et al. (2017) for SN rate calculations, treating the number of spectroscopic classifications as a binomially distributed variable. We plot as our error bars in Figure 9 the bounds containing 68.3% of the probability.

5.1.1. Systematic Uncertainties

Several assumptions were made when determining $E_{\rm spec}$. To ensure that $E_{\rm spec}$ is unbiased, we repeat our analysis, changing the following underlying assumptions:

1. Replacing the Guy_UV2IR SALT2 model with the model of JLA-B14 (Betoule et al. 2014), used in the DES-3YR cosmological analysis, but spanning a narrow wavelength range;
2. Considering the observed rather than fit peak i-band magnitude;
3. Enforcing stricter/less conservative PSNID cuts when determining our photometric sample: i.e., changing (FITPROB$_{\rm Ia}$, PBAYES$_{\rm Ia}$) $>$ (0.01,0.9) to (0.001,0.5) or (0.1,0.99).
4. Enforcing stricter SALT2 cuts when determining our photometric sample: i.e., changing ($|x_1| < 4$, $|c| < 1$) to ($|x_1| < 3$, $|c| < 0.3$).

Our systematic is taken to be the maximum variation in the derived $E_{\rm spec}$ in each magnitude bin. We plot this alongside the statistical uncertainty in Figure 9. Over the entire magnitude range, the systematic uncertainty is comparable to or smaller than the statistical uncertainty.

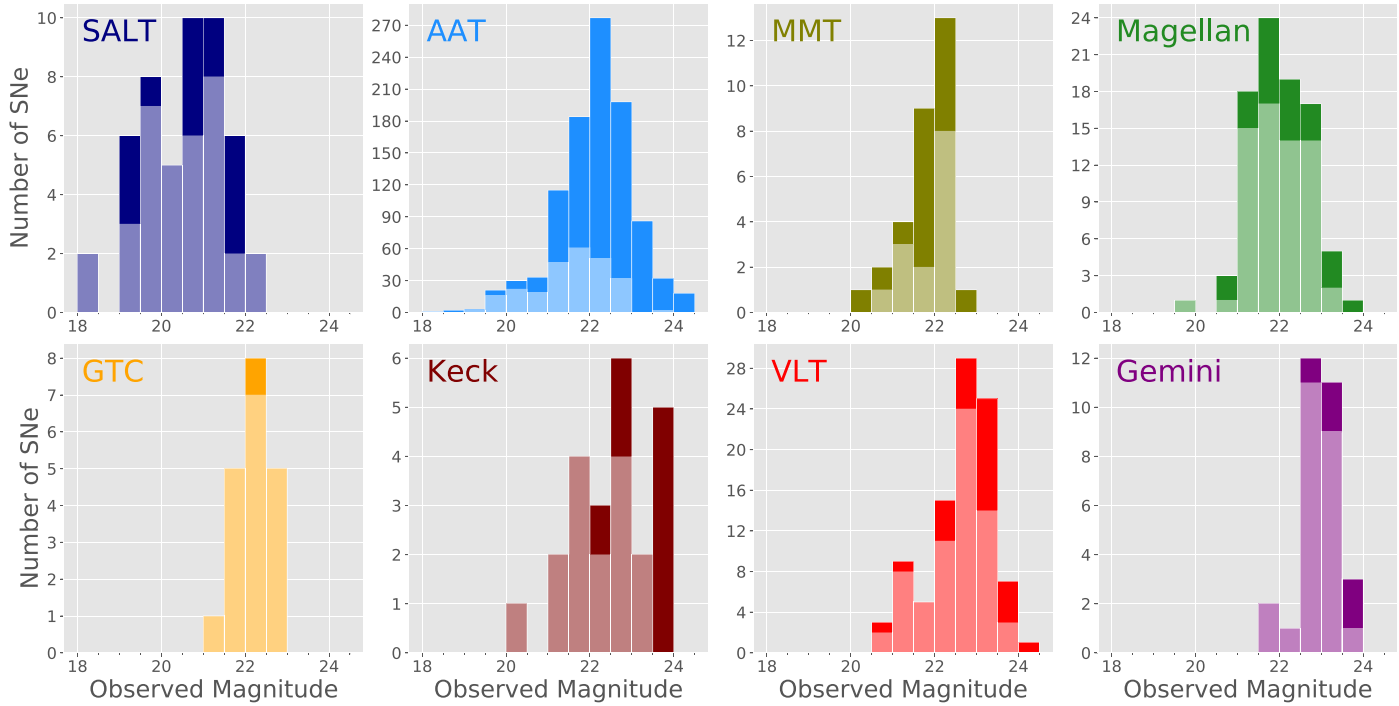

Figure 7. Observed apparent magnitude distributions for transients spectroscopically observed in the first three seasons of DES. Magnitudes are i band for all observatories other than AAT and SALT, which were *r*-band-selected follow-up programs. Distributions are shown separately for each telescope, in order of increasing median apparent magnitude: from $r = 20.8$ for SALT to $i = 23.0$ for Gemini. The lighter shaded histogram in each plot represents the subset of observations that resulted in a successful classification.

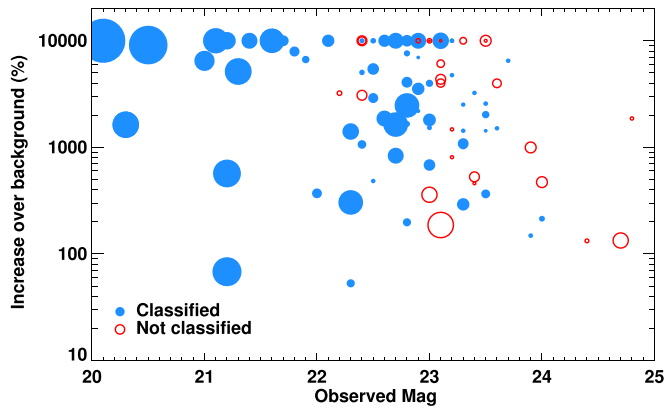

Figure 8. Observed *i*-band magnitude plotted against the percentage increase over background flux for each SN observed by our VLT program. SNe that are > 10,000% the brightness of their background are plotted at this value for purposes of clarity. Successful classifications are shown as blue filled circles, while non-classifications are plotted as red open circles. The size of each point is proportional to the S/N for the spectrum as described in Section 4.5.

5.2. *An Alternative Approach:* E_{spec} *Derived from Simulations*

The "data-driven" $E_{\rm spec}$, derived in Section 5.1, is independent from assumptions on the underlying distribution of SNe Ia but requires assumptions about our ability to accurately photometrically classify SN candidates. Such redshift-free photometric classification may be susceptible to contamination from stripped-envelope SNe (SeSNe; Vincenzi et al. 2019; Möller & de Boissière 2020), thus we also derive $E_{\rm spec}$ using simulated samples as an independent verification. The "model-driven" $E_{\rm spec}$, derived here matches that used in the DES-SN3YR cosmology analysis (Dark Energy Survey Collaboration et al. 2019b).

By simulating DES-SN3YR without any spectroscopic selection (i.e., assuming that $E_{\rm spec} \equiv 1$ independent of magnitude), we can predict the expected magnitude distribution of all SNe Ia in our photometric data—$N_{\rm PhotIa}$ in Equation (1). By dividing the spectroscopic SN Ia sample by this simulated sample as a function of peak *i*-band magnitude, we determine $E_{\rm spec}$ in a model-driven approach.

This approach is insensitive to uncertainties around photometric classification that could bias our data-driven approach, but is instead dependent on an assumed model of SNe Ia. This includes the distribution of SN Ia SALT2 parameters (x_1, c), their rate as a function of redshift, and the intrinsic scatter model that represents the un-modeled variation in the SN Ia Hubble diagram ($\sigma_{\rm int}$). To simulate DES-SN3YR, we use the simulation tool of Kessler et al. (2019), which combines the actual observing pattern of DES-SN with assumptions on the underlying distribution of SNe Ia to produce simulated data sets. For parameters underlying the simulation, we match those used in the DES-SN3YR analysis (Brout et al. 2019b), namely:

1. SALT2 model: Betoule et al. (2014; JLA–B14_LAMOPEN)[86]
2. SN Ia instrinsic scatter model: Guy et al. (2010)
3. SN Ia rates: Perrett et al. (2012)
4. SALT2 parameter distribution: Scolnic & Kessler (2016; Table 1, high-z,G10 row)
5. MW dust maps: Schlafly & Finkbeiner (2011)

[86] This is an extension in wavelength coverage of the JLA-B14 model (Betoule et al. 2014), which would otherwise only use DES-SN *gr* photometry in light-curve fits of low-redshift ($z \leqslant 0.11$) SNe.

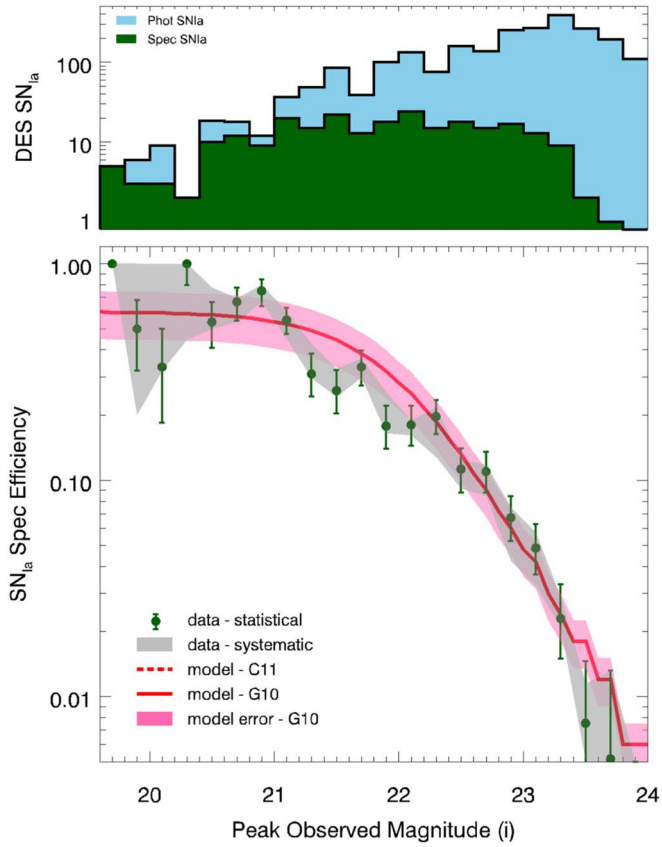

Figure 9. Top: histogram of the number of SNe Ia spectroscopically classified (251; green) and photometrically classified (2634; blue) in this paper, as a function of peak observed i-band magnitude. Bottom: data-driven $E_{\rm spec}$ (green), defined as a function of peak observed i-band magnitude, derived from the data shown in the top plot. Error bars are statistical uncertainties in each bin, and the gray band is our estimated systematic uncertainty, described in Section 5.1. In our analysis we set the efficiency to 1 at $i \leqslant 20.3$ mag to prevent artifacts in our derived μ-bias, as described in the text. The model-driven estimates of $E_{\rm spec}$, described in Section 5.2, are shown as solid and dotted lines depending on the assumed scatter model G10 or C11, respectively. We show the 1σ contour for the G10 derivation only and note that the contours with the C11 model are very similar. The model-driven $E_{\rm spec}$ has an arbitrary normalization, which we scale here to minimize the difference with respect to the data-driven $E_{\rm spec}$.

6. Extinction law: Fitzpatrick (1999)
7. Nuisance parameters: $\alpha = 0.15$, $\beta = 3.1$
8. Cosmology: flat ΛCDM, $\Omega_M = 0.3$, $H_0 = 70$ km s^{-1} Mpc^{-1}

To determine our model-driven $E_{\rm spec}$ we simulate DES-SN with fixed $E_{\rm spec} == 1$ and divide the spectroscopic SN Ia sample by this simulated sample in bins of peak i-band magnitude. The model-driven $E_{\rm spec}$ efficiency ϵ is determined from a sigmoid fit to the binned data,

$$\epsilon\,(i_{\rm peak}) = \frac{s_0}{1 + \exp(s_1 \times i_{\rm peak} - s_2)}, \qquad (2)$$

where s_0, s_1, and s_2 are free parameters determined with `emcee` (Foreman-Mackey et al. 2013). For the fitting, we model data uncertainties using a Poisson distribution. We perform the fit on the data-simulation ratio and then use the sigmoid amplitude, s_0, as the normalization parameter. This allows $E_{\rm spec}$ to asymptote to a constant value for bright transients, go to zero for sufficiently faint transients, and transition smoothly between these two extremes.[87,88]

Table 7
DES "Data-Driven" Spectroscopic Efficiency

Peak Mag(i)	Efficiency	$\sigma_{\rm stat}$	$\sigma_{\rm sys}$
20.3	1.000	+0.000/−0.205	+0.000/−0.556
20.5	0.538	+0.127/−0.131	+0.239/−0.038
20.7	0.667	+0.108/−0.121	+0.026/−0.128
20.9	0.750	+0.094/−0.113	+0.050/−0.083
21.1	0.550	+0.076/−0.078	+0.055/−0.100
21.3	0.309	+0.073/−0.067	+0.119/−0.014
21.5	0.259	+0.062/−0.056	+0.067/−0.018
21.7	0.333	+0.063/−0.060	+0.032/−0.035
21.9	0.178	+0.042/−0.038	+0.078/−0.013
22.1	0.180	+0.040/−0.036	+0.009/−0.019
22.3	0.197	+0.037/−0.034	+0.021/−0.069
22.5	0.113	+0.028/−0.025	+0.012/−0.021
22.7	0.110	+0.025/−0.022	+0.008/−0.025
22.9	0.067	+0.017/−0.015	+0.008/−0.025
23.1	0.049	+0.014/−0.012	+0.009/−0.016
23.3	0.023	+0.010/−0.008	+0.006/−0.002
23.5	0.008	+0.007/−0.004	+0.004/−0.007
23.7	0.005	+0.008/−0.004	+0.008/−0.001

Note. The efficiency is fixed to 1.000 below magnitude 20.3.

Figure 9 shows $E_{\rm spec}$ as determined using this method with the intrinsic scatter on the simulated SNe based on the intrinsic scatter models of Guy et al. (2010; G10) or Chotard et al. (2011; C11) as implemented through the spectral variations defined in Kessler et al. (2013). The assumption of either scatter model results in minimal differences in $E_{\rm spec}$.

The two derivations of $E_{\rm spec}$ are statistically consistent. Using the statistical uncertainties from the data-driven model and the 1σ contour from the model-based derivation, we find $\chi^2/{\rm DoF} = 0.7$. Visible differences between the two estimates of $E_{\rm spec}$ may be due to the assumption of a smooth sigmoid function in the model-dependent approach; while classification efficiency monotonically increases for brighter transients on a given telescope, the strategy of having different telescopes for different targets results in a non-smoothly varying process as shown by the evolution of the data-driven $E_{\rm spec}$.

Having determined $E_{\rm spec}$ using two independent methodologies and shown that they produce consistent results, we now turn to see if these estimates of $E_{\rm spec}$ can replicate the observed distributions of z, x_1, and c for the DES-SN3YR data set in simulated samples.

5.3. Data Comparison to Simulations

The data-driven $E_{\rm spec}$ derived in Section 5.1 comes directly from the observed data and is not dependent on simulations or any assumptions on SN properties. Thus, a realistic simulation of DES-SN that includes this spectroscopic efficiency should recover a spectroscopic SN Ia sample that is consistent with the DES-SN3YR sample both in redshift and as a function of the SN Ia light-curve parameters.

[87] The procedure used to define this selection function is available here https://github.com/anaismoller/DES_selection_function/tree/DES3yr_frozen.
[88] The model-driven $E_{\rm spec}$ is available within the `SNANA` framework as part of the public DES-SN 3YR data release.

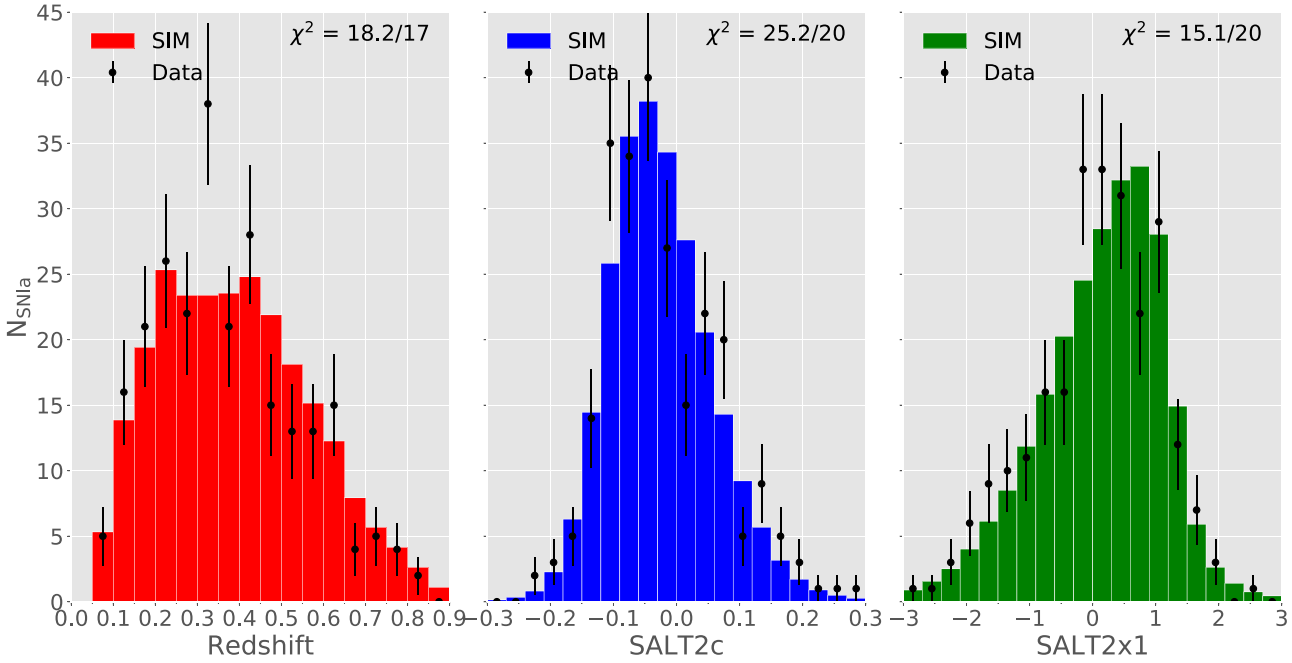

Figure 10. Distributions of redshift, SALT2 x_1, and SALT2 c for both our spectroscopic sample and a DES-like simulation using E_{spec} we derived from the data (and which therefore should be representative of the spectroscopic sample). The simulation is normalized to the number of points in the data histogram and uncertainties on the data are $\sqrt{N}$ statistics. The goodness-of-fit for each histogram is shown as the χ^2 on each plot.

To test the consistency of the data-driven E_{spec} with the DES-SN3YR data set, we simulate DES-SN using the parameters given in Section 5.2 and E_{spec} derived in Section 5.1. To match the DES-SN3YR cosmology analysis (Brout et al. 2019b) we determine the SALT2 parameters for our simulated sample and the DES-SN3YR data set using the JLA–B14 model. Figure 10 shows the binned redshift, x_1, and color distribution for the DES-SN3YR sample compared to our simulated sample, normalized to the same number of SNe Ia as the spectroscopic sample, with uncertainties calculated as $\sqrt{N}$ for the observed data.

There is good agreement between our simulation and the data. We find a χ^2/DoF of 1.07 when considering the distribution of redshift for our simulated sample compared to the DES-SN3YR sample, with $\chi^2/\mathrm{DoF} = 1.26$ for x_1 and 0.76 for color. This does not simply represent a judicious choice of binning; for example, shifting the starting point of our $\Delta c = 0.03$ bins by 0.01 in either direction leads to $\chi^2/\mathrm{DoF} < 1$. A two-sided Kolmogorov–Smirnov (KS) test using the distributions of these parameters, returns p-values of 0.11, 0.38, and 0.16 for z, x_1, and c, respectively, showing no evidence that our simulated and observed data sets arise from different distributions.

In Figure 11 we plot the two-dimensional distribution of derived SALT2 x_1 and c from our spectroscopic sample and compare it to a contour plot derived from a kernel density estimator (KDE) of our simulation. In Figure 12 we show the simulated and measured evolution of SALT2 parameters over the redshift range of our observations. Both plots demonstrate that our data match the trends expected from our simulation with our x_1/c measurements clustered around the peak of the KDE and an increasing (decreasing) trend with redshift or SALT2 x_1 (c). There are some statistically significant differences: an overabundance of observed SNe Ia in low-probability areas of x_1/c space and a trend for lower-than-expected x_1 values at $z < 0.1$, potentially a consequence of brightest, high-x_1 SNe Ia saturating DECam at the lowest redshifts than their fainter, low x_1 counterparts. Overall, it is difficult to state whether these differences are due to small number statistics, signs of unaccounted bias in E_{spec}, whether the intrinsic parameter model for SNe Ia in DES differs from that determined from SDSS+PS1+SNLS data (Scolnic & Kessler 2016) or whether the intrinsic parameters that describe SNe Ia evolve with redshift (Nicolas et al. 2020).

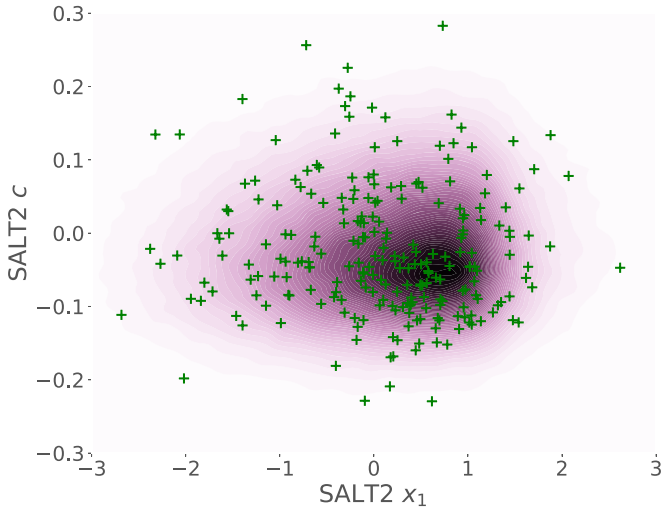

Figure 11. Joint distribution of SALT2 x_1 and c for a DES-like simulation that uses the data-driven E_{spec}. The contours are derived from a kernel density estimator where darker colors represent higher population density. Measured parameters from our spectroscopically confirmed SNe Ia are plotted in green.

The E_{spec} determined in Equation (1) is clearly a simplified description of our strategy. Follow-up decisions and classification efficiency (both of which are combined into E_{spec}) were functions of multiple variables beyond peak magnitude,

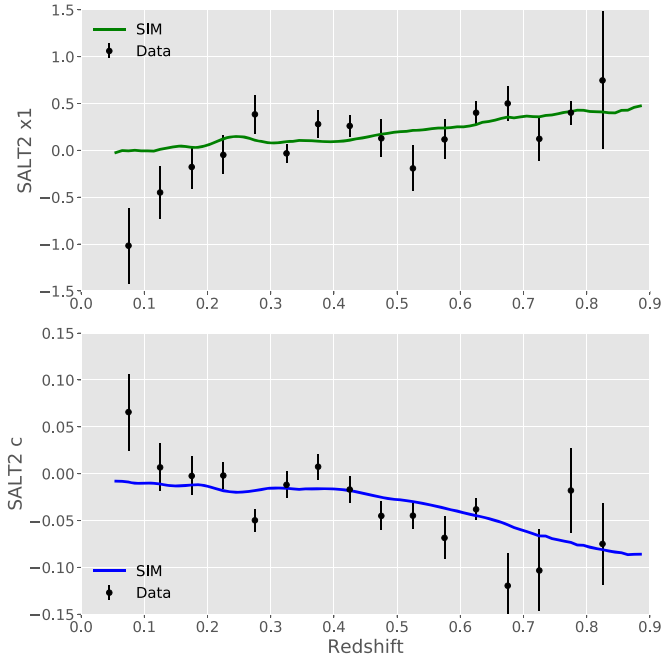

Figure 12. Redshift dependence of SALT2 x_1 and c for a DES-like simulation that uses the data-driven $E_{\rm spec}$. The lines are rolling averages of the simulated parameters, while weighted mean and the standard deviation on the mean are shown for the data, binned by $\Delta z = 0.05$.

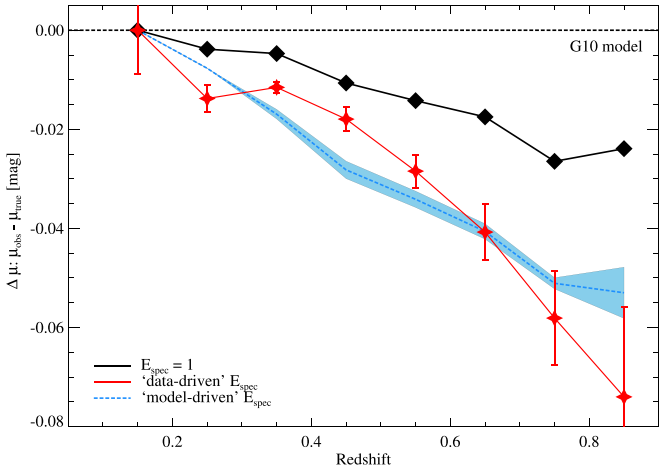

Figure 13. Redshift-dependent bias derived from spectroscopic selection function derivations. The black solid line shows the recovered bias on the distance modulus, μ, derived with perfect spectroscopic efficiency, which reveals the limitations of the survey (and perfect photometric classification). The red line is the μ-bias derived from the data-driven $E_{\rm spec}$, while the blue dashed line shows the model-driven $E_{\rm spec}$. In both cases, 1σ uncertainties are derived by considering maximal and minimal 1σ variations in $E_{\rm spec}$ as shown in Figure 9, and shown as red error bars and a blue band, respectively. All $E_{\rm spec}$'s assume an intrinsic G10 scatter model for consistency.

including host-galaxy mass, local surface brightness, and observed color. We explored adding these variables to the definition of $E_{\rm spec}$, but as shown in this Section, using just a single variable provides an effective description of the full DES-SN3YR spectroscopic sample.

For comparison, we also run a DES-like simulation assuming the model-driven $E_{\rm spec}$, determined in Section 5.2, and again compare the resulting z, x_1, and c distributions to the data using the two-sample KS test. We find the probabilities that the underlying distribution of our simulated samples matches the observed distribution to be 0.02, 0.41, and 0.18, respectively. While the x_1 and c distributions are consistent, there is some evidence for a difference in the redshift distribution, primarily driven by an underabundance of SNe Ia in the simulation compared to data at low z. This underabundance, which peaks at $z \approx 0.25$, is similar in nature but slightly stronger than the underabundance at mid- to low redshifts from the data-driven model, which peaks at $z \approx 0.35$. These results match those found in Brout et al. (2019b) and Kessler et al. (2019).

Having shown that our two, *independently derived* estimates of $E_{\rm spec}$ can replicate the DES-SN3YR data set, we now consider how these deviations affect cosmological constraints derived from the DES-SN3YR data set.

5.4. μ-Bias

The cosmological parameter analysis and measurement of systematic uncertainties for the DES-SN3YR sample in Brout et al. (2019b) uses the model-driven $E_{\rm spec}$ as a baseline. The utility of this approach is clear, as $E_{\rm spec}$ is derived from the same suite of simulations defined by Kessler et al. (2019) and used to quantify the uncertainties in the analysis. It would also be difficult to do a rigorous evaluation of systematic uncertainties owing to the photometrically classified sample used in the data-driven approach. However, the benefit of the data-driven approach is that, being free of the assumptions that go into defining the model of the observed SNe Ia population, it allows for a comparison of $E_{\rm spec}$ that cannot be computed from the simulations alone.

We demonstrate the effects $E_{\rm spec}$ imparts on our observed data in Figure 13, where we show the simulated redshift-dependent bias in distance modulus for various assumptions about our selection effects. For each selection function, we simulate DES-SN using identical input parameters, matching those listed in Section 5.2, only varying the assumed $E_{\rm spec}$. The bias ($\Delta\mu$) is computed as the difference between the "observed" distance modulus ($\mu_{\rm obs}$), derived from fitting each simulated light curve with the JLA-B14 model and determining distances using the simulated nuisance parameters ($\alpha = 0.15$, $\beta = 3.1$) and the true distance modulus ($\mu_{\rm true}$) in bins of redshift using a weighted mean with $\sigma_{\rm int} = 0.066$ as determined in Brout et al. (2019b).

The black solid line in Figure 13 shows the μ-bias that would be expected from a perfect spectroscopic selection (i.e., $E_{\rm spec} = 1$); the depth of the photometry from DES means there would be nearly no bias for a perfectly selected SN Ia sample out to $z \approx 0.3$, smoothly dropping off thereafter to a bias of $\Delta\mu = 0.025$ at $z \approx 0.85$. Refer to Figure 6 for the redshift distribution of the DES-SN3YR subsample.

The data-driven and model-driven functions (shown in Figure 13 in red and blue, respectively) agree on average, differing by <0.007 to $z = 0.75$ and >0.02 mag only at $z > 0.85$, which represents less than 3 percent of the DES-SN3YR sample. The differences can be attributed to the different shapes of the selection functions (Figure 9). The steps and plateaus seen in the data-driven model are due to the binned nature of the data-driven model, while the functional form of the model-driven $E_{\rm spec}$ leads to a simpler redshift evolution: flat at low z and an effectively linear decline thereafter. The difference in μ-bias between the black line and either of the two other lines isolates the effect on the μ-bias due to the spectroscopic selection, distinct from the pipeline

detection efficiency. This demonstrates that the μ-bias due explicitly to $E_{\rm spec}$ lies between 0.01 to 0.03 mag over a wide range of redshift. The difference between the data-driven and model-driven $E_{\rm spec}$'s is consistent with the 1σ statistical fluctuations observed for the model-driven selection function, as shown by the blue shaded region in Figure 13. For the cosmological parameters, Brout et al. (2019b) determined that the selection function has only a minimal impact, finding that variations in the model-driven selection function can cause a shift in the equation-of-state of dark energy, w of 0.001, with $\sigma_w = 0.007$: the ninth largest source of uncertainty. Given the statistical consistency between the data-driven and model-driven selection functions, it is clear that cosmological parameters derived using the data-driven selection function will be entirely consistent with the DES-SN3YR cosmological results (Dark Energy Survey Collaboration et al. 2019b).

6. Summary

In this paper we have presented the survey operations and spectroscopic follow-up observations for the first three years of DES-SN. This includes a detailed overview of the DES-SN observing strategy. On average, a DES season was ∼5.5 months long, with each of our 10 fields observed in *griz* every 7.4 days. The median depth was ∼23.5 mag in the eight shallow fields and ∼24.6 mag in the two deep fields. The median observed FWHM in *griz* for our program was 1.″41/1.″29/1.″17/1.″09.

We described results from our data-processing pipeline, the details of which are mostly contained in other papers (Kessler et al. 2015; Goldstein et al. 2015; Gupta et al. 2016; Morganson et al. 2018). DES-SN recorded 1.21 million real single-epoch, single-filter detections—nearly 400 per image. From these detections, approximately 46,000 SN candidates were identified, which we subsequently narrowed down to 12,015 viable single-season transients. On average we discovered 24 likely SNe per night.

We then presented our live-SN spectroscopy follow-up, consisting of magnitude-limited, faint host, representative, and non-Ia programs. Observations were made on an assortment of telescopes. In total we collected 1385 spectra—1039 of which were from AAT—resulting in 251 classifications of SNe Ia and 56 non-Ia SNe. Our spectroscopically classified SN Ia sample spans a redshift range of $0.017 < z < 0.85$, forming the basis of the DES-SN3YR data set.

Finally, we derived the effective spectroscopic selection function ($E_{\rm spec}$) from our large, diverse follow-up program that resulted in our classified sample of DES SNe Ia. One method is data-driven, relying on photometric classification to determine the fraction of real SN Ia in our data while the model-driven method relies on simulations of our survey. The two independently derived estimates of $E_{\rm spec}$ are consistent over a wide magnitude range and produce distributions of z, x_1, and c that match the DES-SN3YR data set when simulating DES-SN. We show the resulting redshift-dependent bias $E_{\rm spec}$ imparts upon the measured distance modulus for each method and remark on how this is a subdominant systematic error on the resulting cosmology analysis, as shown in the companion paper Dark Energy Survey Collaboration et al. (2019b).

This paper has gone through internal review by the DES collaboration.

Based in part on data acquired through the Australian Astronomical Observatory under program ATAC A/2013B/12. We acknowledge the traditional owners of the land on which the AAT stands, the Gamilaraay people, and pay our respects to elders past and present. Based on observations obtained at the Gemini Observatory, which is operated by the Association of Universities for Research in Astronomy, Inc., under a cooperative agreement with the NSF on behalf of the Gemini partnership: the National Science Foundation (United States), the National Research Council (Canada), CONICYT (Chile), Ministerio de Ciencia, Tecnología e Innovación Productiva (Argentina), and Ministério da Ciência, Tecnologia e Inovação (Brazil). Observations with Gemini were obtained under NOAO programs 2013A-0373 and 2015B-0197, corresponding to GN-2013B-Q-55, GS-2013B-Q-45, GS-2015B-Q-7, GN-2015B-Q-10, as well as GS-2015B-Q-8 under a Chilean program. Based on observations made with the Gran Telescopio Canarias (GTC), installed at the Spanish Observatorio del Roque de los Muchachos of the Instituto de Astrofísica de Canarias, in the island of La Palma. Observations with GTC were made under programs GTC77-13B, GTC70-14B, and GTC101-15B. Some of the data presented herein were obtained at the W. M. Keck Observatory, which is operated as a scientific partnership among the California Institute of Technology, the University of California and the National Aeronautics and Space Administration (NASA). The Observatory was made possible by the generous financial support of the W. M. Keck Foundation. Observations with Keck were made under programs U063-2013B, U021-2014B, U048-2015B, and U038-2016A. The authors wish to recognize and acknowledge the very significant cultural role and reverence that the summit of Maunakea has always had within the indigenous Hawaiian community. We are most fortunate to have the opportunity to conduct observations from this mountain. This paper includes data gathered with the 6.5 meter Magellan Telescopes located at Las Campanas Observatory, Chile, partially through program CN2015B-89. Observations reported here were obtained at the MMT Observatory, a joint facility of the Smithsonian Institution and the University of Arizona, under programs 2014c-SAO-4, 2015a-SAO-12, 2015c-SAO-21. Some of the observations reported in this paper were obtained with the Southern African Large Telescope (SALT) under programs 2013-1-RSA_OTH-023, 2013-2-RSA_OTH-018, 2014-1-RSA_OTH-016, 2014-2-SCI-070, 2015-1-SCI-063, and 2015-2-SCI-061. Based on observations collected at the European Southern Observatory under ESO programmes 093.A-0749(A), 094.A-0310(B), 095.A-0316(A), 096.A-0536(A), 095.D-0797(A). Based on observations obtained at the Southern Astrophysical Research (SOAR) telescope, which is a joint project of the Ministério da Ciência, Tecnologia, Inovações e Comunicações (MCTIC) do Brasil, the U.S. National Optical Astronomy Observatory (NOAO), the University of North Carolina at Chapel Hill (UNC), and Michigan State University (MSU). SOAR observations obtained under program 2014B-0205. Research at Lick Observatory is partially supported by a generous gift from Google.

The Southampton group acknowledges support from EU-FP7/ERC grant [615929]. MS acknowledges funding from the European Research Council (ERC) under the European Union? s Horizon 2020 research and innovation program (grant agreement No. 759194—USNAC). The Penn group was supported by DOE grant DE-FOA-0001358 and NSF grant AST-1517742. This research used resources of the National

Energy Research Scientific Computing Center (NERSC), a DOE Office of Science User Facility supported by the Office of Science of the U.S. Department of Energy under Contract No. DE-AC02-05CH11231. A.V.F.'s group at U.C. Berkeley is grateful for financial assistance from NSF grant AST-1211916, the Christopher R. Redlich Fund, Gary and Cynthia Bengier, the TABASGO Foundation, and the Miller Institute for Basic Research in Science. The UCSC team is supported in part by NASA grants 14-WPS14-0048, NNG16PJ34G, NNG17PX03C, NSF grants AST-1518052 and AST-1815935, the Gordon & Betty Moore Foundation, the Heising-Simons Foundation, and by fellowships from the Alfred P. Sloan Foundation and the David and Lucile Packard Foundation to R.J.F. SGG acknowledges support by FCT under Project CRISP PTDC/FIS-AST-31546 and UIDB/00099/2020. L.G. was funded by the European Union's Horizon 2020 research and innovation program under the Marie Skłodowska-Curie grant agreement No. 839090. This work has been partially supported by the Spanish grant PGC2018-095317-B-C21 within the European Funds for Regional Development (FEDER). Support for AC was provided by ANID, through the Millennium Science Initiative grant ICN12_009 (MAS) and by grant Basal CATA PFB 06/09.

Funding for the DES Projects has been provided by the U.S. Department of Energy, the U.S. National Science Foundation, the Ministry of Science and Education of Spain, the Science and Technology Facilities Council of the United Kingdom, the Higher Education Funding Council for England, the National Center for Supercomputing Applications at the University of Illinois at Urbana-Champaign, the Kavli Institute of Cosmological Physics at the University of Chicago, the Center for Cosmology and Astro-Particle Physics at the Ohio State University, the Mitchell Institute for Fundamental Physics and Astronomy at Texas A&M University, Financiadora de Estudos e Projetos, Fundação Carlos Chagas Filho de Amparo à Pesquisa do Estado do Rio de Janeiro, Conselho Nacional de Desenvolvimento Científico e Tecnológico and the Ministério da Ciência, Tecnologia e Inovação, the Deutsche Forschungsgemeinschaft and the Collaborating Institutions in the Dark Energy Survey.

The Collaborating Institutions are Argonne National Laboratory, the University of California at Santa Cruz, the University of Cambridge, Centro de Investigaciones Energéticas, Medioambientales y Tecnológicas-Madrid, the University of Chicago, University College London, the DES-Brazil Consortium, the University of Edinburgh, the Eidgenössische Technische Hochschule (ETH) Zürich, Fermi National Accelerator Laboratory, the University of Illinois at Urbana-Champaign, the Institut de Ciències de l'Espai (IEEC/CSIC), the Institut de Física d'Altes Energies, Lawrence Berkeley National Laboratory, the Ludwig-Maximilians Universität München and the associated Excellence Cluster Universe, the University of Michigan, NFS's NOIRLab, the University of Nottingham, The Ohio State University, the University of Pennsylvania, the University of Portsmouth, SLAC National Accelerator Laboratory, Stanford University, the University of Sussex, Texas A&M University, and the OzDES Membership Consortium.

Based in part on observations at Cerro Tololo Inter-American Observatory at NSF?s NOIRLab (NOIRLab Prop. ID 2012B-0001; PI: J. Frieman), which is managed by the Association of Universities for Research in Astronomy (AURA) under a cooperative agreement with the National Science Foundation.

The DES data management system is supported by the National Science Foundation under Grant Numbers AST-1138766 and AST-1536171. The DES participants from Spanish institutions are partially supported by MICINN under grants ESP2017-89838, PGC2018-094773, PGC2018-102021, SEV-2016-0588, SEV-2016-0597, and MDM-2015-0509, some of which include ERDF funds from the European Union. IFAE is partially funded by the CERCA program of the Generalitat de Catalunya. Research leading to these results has received funding from the European Research Council under the European Union's Seventh Framework Program (FP7/2007-2013) including ERC grant agreements 240672, 291329, and 306478. We acknowledge support from the Brazilian Instituto Nacional de Ciência e Tecnologia (INCT) e-Universe (CNPq grant 465376/2014-2).

Facilities: AAT (AAOmega), Blanco (DECam), Gemini: North (GMOS), Gemini:South (GMOS), GTC (OSIRIS), Keck:I (LRIS), Keck:II (DEIMOS), Magellan:Baade (LDSS2 imaging spectrograph), Magellan:Clay (LDSS2 imaging spectrograph), MMT (Blue Channel spectrograph), NTT (EFOSC2), SALT (RSS), Shane (Kast Double spectrograph), SOAR, VLT: Kueyen (X-Shooter).

Appendix

Observational data and results obtained by DES-SN during the first three years of survey operations. Table A1 shows details (target, instrument, date, brightness) of all spectroscopic observations taken for the DES3YR analysis, while Table A2

Table A1
Spectroscopic Observing Log: DES-SN Y1-Y3

Transient Name	SNID[a]	Telescope	Instrument	Obs Date [UT]	Obs Date [MJD]	Observed[b] Mag$_i$	% Flux[c] Increase
DES13C1c	1246286	AAT	AAOmega-2dF	2013 Oct 01	56566	22.3	335.4
DES13C1d	1254622	AAT	AAOmega-2dF	2013 Oct 01	56566	23.7	29.8
DES13C1e	1246275	AAT	AAOmega-2dF	2013 Oct 01	56566	21.9	151.3
DES13C1ehq	1272887	AAT	AAOmega-2dF	2013 Oct 01	56566	…	…
DES13C1eie	1264730	AAT	AAOmega-2dF	2013 Nov 30	56626	24.1	21.3
DES13C1eie	1264730	AAT	AAOmega-2dF	2013 Dec 01	56627	24.1	21.3
DES13C1feu	1251839	SALT	RSS	2013 Oct 08	56573	19.9	238.9
DES13C1feu	1251839	AAT	AAOmega-2dF	2013 Oct 30	56595	20.9	92.8
DES13C1feu	1251839	AAT	AAOmega-2dF	2013 Nov 02	56598	21.2	71.2
DES13C1feu	1251839	AAT	AAOmega-2dF	2013 Nov 30	56626	22.0	35.8
DES13C1feu	1251839	AAT	AAOmega-2dF	2013 Dec 01	56627	22.0	35.8

Notes. This table is available in full as part of the DES-SN3YR data release: https://des.ncsa.illinois.edu/releases/sn.
[a] Matches value used in the DES-SN3YR cosmology analysis (Dark Energy Survey Collaboration et al. 2019b).
[b] Apparent magnitude from DES-SN observation on the epoch $t_{\rm phot}$ closest to the time of spectroscopic follow-up $t_{\rm spec}$. Column is blank for entries where no DES-SN photometric data point, passing `DiffImg`, is available within 21 days of observation.
[c] Brightness of target at time of observation relative to the surface brightness of the background. Column is blank for entries where no DES-SN photometric data point, passing `DiffImg`, is available within 21 days of observation.

Table A2
Spectroscopically Confirmed SNe in the DES-SN3YR Sample

Transient Name	SNID	RA (J2000)	DEC	Classification	z
DES13C2bxd	1247673	54.5104	−29.1570	SNIc	0.04042
DES13C3dgs	1248677	53.6462	−28.1270	SNIa	0.35067
DES13C3ui	1248844	51.6694	−28.0652	SNII	0.06667
DES13E1ao	1248907	7.2814	−43.1410	SNIa	0.17140
DES13S2cmm	1249305	40.6367	−1.3583	SLSN-I	0.66229
DES13C2dyc	1249851	55.2180	−29.4000	SNIa	0.21591
DES13S1qv	1250017	43.1937	−0.1275	SNIa	0.183
DES13X3fca	1251622	36.0173	−4.3570	SNII	0.09615
DES13C1feu	1251839	53.2667	−26.9648	SNIc	0.05982

Note. This table is available in full as part of the DES-SN3YR data release: https://des.ncsa.illinois.edu/releases/sn.

lists the aggregated classifications and redshifts for transients discovered by DES-SN. Full versions of these tables can be found as part of the DES-3YR data release.[89]

ORCID iDs

M. Smith https://orcid.org/0000-0002-3321-1432
M. Sullivan https://orcid.org/0000-0001-9053-4820
D. Brooks https://orcid.org/0000-0002-8458-5047
E. Gaztanaga https://orcid.org/0000-0001-9632-0815
G. Tarle https://orcid.org/0000-0003-1704-0781

References

Adelman-McCarthy, J. K., Agüeros, M. A., Allam, S. S., et al. 2007, ApJS, 172, 634
Angus, C. R., Smith, M., Sullivan, M., et al. 2019, MNRAS, 487, 2215
Betoule, M., Kessler, R., Guy, J., et al. 2014, A&A, 568, A22
Blondin, S., & Tonry, J. L. 2007, ApJ, 666, 1024
Brout, D., Sako, M., Scolnic, D., et al. 2019a, ApJ, 874, 106
Brout, D., Scolnic, D., Kessler, R., et al. 2019b, ApJ, 874, 150
Childress, M. J., Lidman, C., Davis, T. M., et al. 2017, MNRAS, 472, 273
Chotard, N., Gangler, E., Aldering, G., et al. 2011, A&A, 529, L4
Conley, A., Guy, J., Sullivan, M., et al. 2011, ApJS, 192, 1
Contreras, C., Hamuy, M., Phillips, M. M., et al. 2010, AJ, 139, 519
Croom, S., Saunders, W., & Heald, R. 2004, AAONw, 106, 12
Dark Energy Survey Collaboration, Abbott, T., Abdalla, F. B., et al. 2016, MNRAS, 460, 1270
Dark Energy Survey Collaboration, Abbott, T. M. C., Alarcon, A., et al. 2019a, PhRvL, 122, 171301
Dark Energy Survey Collaboration, Abbott, T. M. C., Allam, S., et al. 2019b, ApJL, 872, L30
de Jaeger, T., Galbany, L., González-Gaitán, S., et al. 2020, MNRAS, 495, 4860
Diehl, H. T., Abbott, T. M. C., Annis, J., et al. 2014, Proc. SPIE, 9149, 91490V
Filippenko, A. V. 1982, PASP, 94, 715
Fitzpatrick, E. L. 1999, PASP, 111, 63
Flaugher, B., Diehl, H. T., Honscheid, K., et al. 2015, AJ, 150, 150
Foley, R. J., Sanders, N. E., & Kirshner, R. P. 2011, ApJ, 742, 89
Foley, R. J., Scolnic, D., Rest, A., et al. 2018, MNRAS, 475, 193
Foreman-Mackey, D., Hogg, D. W., Lang, D., & Goodman, J. 2013, PASP, 125, 306
Frieman, J. A., Bassett, B., Becker, A., et al. 2008, AJ, 135, 338
Frohmaier, C., Sullivan, M., Nugent, P. E., Goldstein, D. A., & DeRose, J. 2017, ApJS, 230, 4
Ganeshalingam, M., Li, W., Filippenko, A. V., et al. 2010, ApJS, 190, 418
Giacconi, R., Rosati, P., Tozzi, P., et al. 2001, ApJ, 551, 624
Goldstein, D. A., D'Andrea, C. B., Fischer, J. A., et al. 2015, AJ, 150, 82
Gupta, R. R., Kuhlmann, S., Kovacs, E., et al. 2016, AJ, 152, 154
Gutiérrez, C. P., Anderson, J. P., Hamuy, M., et al. 2017, ApJ, 850, 89
Guy, J., Sullivan, M., Conley, A., et al. 2010, A&A, 523, A7

[89] https://des.ncsa.illinois.edu/releases/sn

Hamuy, M., Phillips, M. M., Suntzeff, N. B., et al. 1996, AJ, 112, 2408
Hicken, M., Challis, P., Jha, S., et al. 2009, ApJ, 700, 331
Hicken, M., Challis, P., Kirshner, R. P., et al. 2012, ApJS, 200, 12
Hinton, S. R., Davis, T. M., Kim, A. G., et al. 2019, ApJ, 876, 15
Howell, D. A., Sullivan, M., Perrett, K., et al. 2005, ApJ, 634, 1190
Jarvis, M. J., Bonfield, D. G., Bruce, V. A., et al. 2013, MNRAS, 428, 1281
Jha, S., Kirshner, R. P., Challis, P., et al. 2006, AJ, 131, 527
Kelly, P. L., Hicken, M., Burke, D. L., Mandel, K. S., & Kirshner, R. P. 2010, ApJ, 715, 743
Kessler, R., Bernstein, J. P., Cinabro, D., et al. 2009, PASP, 121, 1028
Kessler, R., Brout, D., D'Andrea, C. B., et al. 2019, MNRAS, 485, 1171
Kessler, R., Guy, J., Marriner, J., et al. 2013, ApJ, 764, 48
Kessler, R., Marriner, J., Childress, M., et al. 2015, AJ, 150, 172
Kessler, R., & Scolnic, D. 2017, ApJ, 836, 56
Krisciunas, K., Contreras, C., Burns, C. R., et al. 2017, AJ, 154, 211
Lasker, J., Kessler, R., Scolnic, D., et al. 2019, MNRAS, 485, 5329
Lidman, C., Tucker, B. E., Davis, T. M., et al. 2020, MNRAS, 496, 19
Liu, Y.-Q., Modjaz, M., Bianco, F. B., & Graur, O. 2016, ApJ, 827, 90
Lonsdale, C. J., Smith, H. E., Rowan-Robinson, M., et al. 2003, PASP, 115, 897
Macaulay, E., Nichol, R. C., Bacon, D., et al. 2019, MNRAS, 486, 2184
Modjaz, M., Liu, Y. Q., Bianco, F. B., & Graur, O. 2016, ApJ, 832, 108
Möller, A., & de Boissière, T. 2020, MNRAS, 491, 4277
Morganson, E., Gruendl, R. A., Menanteau, F., et al. 2018, PASP, 130, 074501
Neilsen, E., & Annis, J. 2014, in ASP Conf. Ser. 485, Astronomical Data Analysis Software and Systems XXIII, ed. N. Manset & P. Forshay (San Francisco, CA: ASP), 77
Nicolas, N., Rigault, M., Copin, Y., et al. 2020, arXiv:2005.09441
Pan, Y. C., Foley, R. J., Smith, M., et al. 2017, MNRAS, 470, 4241
Papadopoulos, A., D'Andrea, C. B., Sullivan, M., et al. 2015, MNRAS, 449, 1215
Perlmutter, S., Aldering, G., Goldhaber, G., et al. 1999, ApJ, 517, 565
Perrett, K., Sullivan, M., Conley, A., et al. 2012, AJ, 144, 59
Pierre, M., Valtchanov, I., Altieri, B., et al. 2004, JCAP, 2004, 011
Pursiainen, M., Childress, M., Smith, M., et al. 2018, MNRAS, 481, 894
Quimby, R. M., De Cia, A., Gal-Yam, A., et al. 2018, ApJ, 855, 2
Rest, A., Scolnic, D., Foley, R. J., et al. 2014, ApJ, 795, 44
Riess, A. G., Filippenko, A. V., Challis, P., et al. 1998, AJ, 116, 1009
Riess, A. G., Kirshner, R. P., Schmidt, B. P., et al. 1999, AJ, 117, 707
Riess, A. G., Press, W. H., & Kirshner, R. P. 1996, ApJ, 473, 88
Riess, A. G., Rodney, S. A., Scolnic, D. M., et al. 2018, ApJ, 853, 126
Rowan-Robinson, M., Lari, C., Perez-Fournon, I., et al. 2004, MNRAS, 351, 1290
Sako, M., Bassett, B., Becker, A. C., et al. 2018, PASP, 130, 064002
Sako, M., Bassett, B., Connolly, B., et al. 2011, ApJ, 738, 162
Sánchez, C., Carrasco Kind, M., Lin, H., et al. 2014, MNRAS, 445, 1482
Schlafly, E. F., & Finkbeiner, D. P. 2011, ApJ, 737, 103
Scolnic, D., & Kessler, R. 2016, ApJL, 822, L35
Scolnic, D. M., Jones, D. O., Rest, A., et al. 2018, ApJ, 859, 101
Silverman, J. M., Foley, R. J., Filippenko, A. V., et al. 2012, MNRAS, 425, 1789
Smith, M., Nichol, R. C., Dilday, B., et al. 2012, ApJ, 755, 61
Smith, M., Sullivan, M., D'Andrea, C. B., et al. 2016, ApJL, 818, L8
Smith, M., Sullivan, M., Nichol, R. C., et al. 2018, ApJ, 854, 37
Smith, M., Sullivan, M., Wiseman, P., et al. 2020, MNRAS, 494, 4426
Stahl, B. E., Zheng, W., de Jaeger, T., et al. 2019, MNRAS, 490, 3882
Stritzinger, M. D., Phillips, M. M., Boldt, L. N., et al. 2011, AJ, 142, 156
Sullivan, M., Conley, A., Howell, D. A., et al. 2010, MNRAS, 406, 782
Sullivan, M., Le Borgne, D., Pritchet, C. J., et al. 2006, ApJ, 648, 868
Suzuki, N., Rubin, D., Lidman, C., et al. 2012, ApJ, 746, 85
Tonry, J. L., Stubbs, C. W., Lykke, K. R., et al. 2012, ApJ, 750, 99
Vincenzi, M., Sullivan, M., Firth, R. E., et al. 2019, MNRAS, 489, 5802
Williams, S. C., Hook, I. M., Hayden, B., et al. 2020, MNRAS, 495, 3859
Williamson, M., Modjaz, M., & Bianco, F. B. 2019, ApJL, 880, L22
Yuan, F., Lidman, C., Davis, T. M., et al. 2015, MNRAS, 452, 3047